arXiv:1603.07429v1 [astro-ph.HE] 24 Mar 2016

Comprehensive study of the X-ray flares from gamma-ray bursts observed by *Swift*

Shuang-Xi Yi[1,2], Shao-Qiang Xi[4], Hai Yu[2,3], F. Y. Wang[2,3], Hui-Jun Mu[5], Lian-Zhong Lü[6,7] & En-Wei Liang[6,7]

[1]*College of Physics and Engineering, Qufu Normal University, Qufu 273165, China;*
[2]*School of Astronomy and Space Science, Nanjing University, Nanjing 210093, China; fayinwang@nju.edu.cn*
[3]*Key laboratory of Modern Astronomy and Astrophysics (Nanjing University), Nanjing 210093, China*
[4]*Department of Mathematics and Physics, Officers College of CAPF, Chengdu, 610213, China;*
[5]*Department of Astronomy and Institute of Theoretical Physics and Astrophysics, Xiamen University, Xiamen, Fujian 361005, China;*
[6]*GXU-NAOC Center for Astrophysics and Space Sciences, Department of Physics, Guangxi University, Nanning 530004; lew@gxu.edu.cn*
[7]*Guangxi Key Laboratory for the Relativistic Astrophysics, Nanning 530004, China.*

ABSTRACT

X-ray flares are generally supposed to be produced by the later central engine activities, and may share the similar physical origin with prompt emission of gamma-ray bursts (GRBs). In this paper, we have analyzed all significant X-ray flares from the GRBs observed by *Swift* from April 2005 to March 2015. The catalog contains 468 bright X-ray flares, including 200 flares with redshifts. We obtain the fitting results of X-ray flares, such as start time, peak time, duration, peak flux, fluence, peak luminosity, and mean luminosity. The peak luminosity decreases with peak time, following a power-law behavior $L_p \propto T_{peak,z}^{-1.27}$. The flare duration increases with peak time. The 0.3-10 keV isotropic energy of X-ray flares distribution is a lognormal peaked at $10^{51.2}$ erg. We also study the frequency distributions of flare parameters, including energies, durations, peak fluxes, rise times, decay times and waiting times. Power-law distributions of energies, durations, peak fluxes, and waiting times are found in GRB X-ray flares and solar flares. These distributions could be well explained by a fractal-diffusive, self-organized criticality model. Some theoretical models basing on magnetic reconnection have been proposed to explain X-ray flares. Our result shows that the relativistic jets of GRBs may be Poynting-flux dominated.

Subject headings: gamma rays: general — radiation mechanism: non-thermal

1. Introduction

X-ray flare is one of the most common phenomena in the afterglow phase of gamma-ray burst (GRBs) in the *Swift* satellite era (Burrows et al. 2005; Falcone et al. 2006; Zhang et al. 2006; Nousek et al. 2006). There are about one-third of *Swift* GRBs with remarkable X-ray flares. X-ray flares have been observed in both long and short GRBs (Romano et al. 2006; Falcone et al. 2006; Campana et al. 2006; Margutti et al. 2011). Generally, the X-ray flare shows sharp rise and sharp decay. They usually happens at $10^2 - 10^5$ s after the prompt emission (Falcone et al. 2007; Chincarini et al. 2007, 2010). The fluences of most X-ray flares are smaller than the prompt emission observed by *Swift/BAT*. Their average fluence is about 10 percent of the prompt emission statistically (Falcone et al. 2007; Chincarini et al. 2010). From the temporal behavior and spectral property, it is believed that the X-ray flare is from a distinct emission mechanism, which is different from the underlying afterglow emission. While the temporal behavior of flares is very similar to that of prompt emission pulses. Therefore, X-ray flares may have the same physical origin as the prompt pulses of GRBs (Burrows et al. 2005; Falcone et al. 2006, 2007; Zhang et al. 2006; Nousek et al. 2006; Liang et al. 2006; Chincarini et al. 2007, 2010; Hou et al. 2013; Wu et al. 2013; Yi et al. 2015a). Both X-ray flares and GRBs are powered by the central engine activities, therefore the properties of X-ray flares can provide an important clue to understand the mechanism of GRB phenomenon. Some theoretical models have been proposed, such as fragmentation of the collapsing star (King et al. 2005) , fragmentation of the accretion disk (Perna et al. 2006), intermittent accretion behavior caused by a time variable magnetic barrier (Proga & Zhang 2006), magnetic reconnection from a post-merger millisecond pulsar (Dai et al. 2006), and magnetic dissipation in a decelerating shell (Giannios 2006).

Some surveys on the X-ray flares of GRBs observed by *Swift* have been carried out. The studies by Falcone et al. (2007) and Chincarini et al. (2007) selected dozens of flares in the early period of *Swift*. They fitted the X-ray flare with a broken power-law or multiple broken power-law functions, and obtained the fitting parameters of X-ray flares. These studies suggested that flares are produced by late activities of central engine. Follow-up studies with new sample of flares indicated that X-ray flares have some correlations among the flare's parameters (Chincarini et al. 2010; Bernardini et al. 2011; Swenson & Roming 2014). They confirmed that the late-time internal dissipation origin seems the most promising explanation for flares. Margutti et al. (2011) studied X-ray flare candidates in short GRBs, and found that short GRB flares show similar observational properties of long ones after accounting for the central engine time-scales and energy budget. Besides that, Li et al. (2012) also investigated 24 optical flares from 19 GRBs. They suggested that, similar to the X-ray flares, the optical flares are related to the erratic behavior of the central engine. Guidorzi et al. (2015) found that the waiting time distributions of prompt pulses and X-ray flares show

a similar power-law behavior.

X-ray flares are the common astrophysical phenomena throughout the universe. Interestingly, Wang & Dai (2013) compiled 83 GRB flares and 11595 solar hard X-ray flares from *RHESSI* during 2002-2007 and performed a statistical comparison between them. They found the energy, duration, and waiting-time distributions of X-ray flares are similar to those of solar flares, which suggest a similar physical origin of the both events. This result is supported by later numerical simulations (Harko et al. 2015). Harko et al. (2015) numerically investigated the possibility that self-organized criticality (SOC) appears in a one-dimensional magnetized flow, which can be applied to GRB X-ray flares. Wang et al. (2015) studied the energy, duration and waiting time distributions of X-ray flares from Swift J1644+57 (Burrows et al. 2011), Galactic center black hole Sgr A* (Neilsen et al. 2013), and M87 (Harris et al. 2009; Abramowski et al. 2012). These distributions of X-ray flares in different systems show similar power-law distributions. So X-ray flares from astrophysical systems with spatial and mass scales different by many orders of magnitudes show similar behavior, which may indicate that they have similar physical origin.

In this paper, we analyse the ten-year X-ray flare data of *Swift/XRT* until the end of March 2015, and study the distributions of energy, duration, waiting time, rise time, decay time, peak time and peak flux. This paper is organized as follows. In Section 2, we derive the GRB X-ray flare data from *Swift/XRT*, and present the fitting results. In section 3, we study some correlations between parameters of X-ray flares. The distributions of GRB X-ray flares and solar flares are discussed in Section 4. Conclusions and discussion are given in Section 5. A concordance cosmology with parameters $H_0 = 71$ km s $^{-1}$ Mpc^{-1}, $\Omega_M = 0.30$, and $\Omega_\Lambda = 0.70$ is adopted in all part of this work.

2. Data Analysis

Since X-ray flares could be happened at any time of the afterglow phase, the X-ray light curves usually contains one or more power-law segments along with some flares. The mix of different components makes the diverse X-ray afterglow light curves. Here we mainly focus on the flare emission. We extensively search for the remarkable feature of pulses at the GRB X-ray afterglow phase. We consider all the *Swift* GRBs observed between 2005 April and 2015 March, and select 199 GRBs during this period. These X-ray flares generally contain a complete structure, including the remarkable rising and decaying phase. These flares are clearly distinguishable from the underlying continuum emission. We will also apply empirical functions to fit the flare and the underlying component. Small fluctuations around flare have not been identified as flares. The total number of bright X-ray flares is 468, including 200

flares with redshifts. Most GRBs contain a single or several flares. But some of them have more than ten flares, such as GRBs 100212A and 100728A.

The 0.3-10 keV X-ray light curves of GRBs are taken from the website of *Swift/XRT* (Evans et al. 2007, 2009) [1]. We fit the flare with a smooth broken power-law function (Li et al. 2012)

$$F_1(t) = F_{01}\left[\left(\frac{t}{t_b}\right)^{\alpha_1\omega} + \left(\frac{t}{t_b}\right)^{\alpha_2\omega}\right]^{-\frac{1}{\omega}}, \quad (1)$$

and fit the underlying continuum with a power-law function (or broken power-law function)

$$F_2(t) = F_{02}t^{-\alpha_3}, \quad (2)$$

where α_1, α_2 and α_3 are the temporal slopes, t_b is the break time, and ω represents the sharpness of the peak of the light curve component. This method is very similar to the fitting method of Chincarini et al. (2007, 2010). The two examples of the best-fitting flares are shown in Figure 1. From this figure, we can see that the flares of GRB 060111A and GRB 080320 are well fitted. The fitting parameters of flares, such as the start time, peak time, end time, peak flux, fluence, peak luminosity and isotropic energy, are shown in Table 1.

Table 1 consists of 468 bright X-ray flares, including 200 flares with redshifts. The time parameters of flares are derived as follows. The rise time can be obtained by $T_{rise} = T_{peak} - T_{start}$, the decay time $T_{decay} = T_{end} - T_{peak}$ and the duration time $T_{Duration} = T_{end} - T_{start}$, where T_{start}, T_{peak} and T_{end} are the start time, peak time and end time of flares, respectively. The T_{start} and T_{end} are derived from fitting temporal power-law curves to the rise and decay portions of the flares. The points on the light curve where these power laws intersect the underlying decay curve power law are defined as T_{start} and T_{end}. The definition is the same as Falcone et al. (2007). However, similar as the definition of duration of prompt emission, the time interval during which the integrated counts of a burst go from 5% to 95% of the total integrated counts is more reasonable. The waiting time is defined as $T_{waiting} = T_{start,i+1} - T_{start,i}$, where $T_{start,i+1}$ is the observed start time of the $i+1th$ flare, and $T_{start,i}$ is the observed start time of the ith flare. All the flare properties should be transferred into the source frame if they have redshift measurements in the following analysis. For the first flare appearing in X-ray afterglow, the rest-frame waiting time is taken as $T_{start}/(1+z)$. In the case of multiple flares, some flares may occur during the activity of other flares. The waiting time can also defined as above, because the start times of these flares are different. This definition of waiting time is widely used in geophysics (e.g., Omori 1895), magnetospheric

[1] http://www.swift.ac.uk/xrt_curves/

physics (e.g., Chapman et al. 1998), solar physics (e.g., Crosby 1996; Wheatland et al. 1998;), and astrophysics (e.g., Negoro et al. 1995; Wang & Dai 2013). An extensive review on waiting time can be found in chapter 5 of Aschwanden (2011). The isotropic energy of flare in the 0.3-10 keV band can be obtain by $E_{x,iso} = 4\pi D_L^2 S_F/(1+z)$, where z is the redsihft, D_L is the luminosity distance, and S_F is the fluence of flare. The flare fluence S_F is calculated by integrating the corresponding fitting smooth broken power law function (equation (1)) from the start time to the end time of the flare in the 0.2-10 keV energy band. The underlying continuum has been subtracted. The peak luminosity and mean luminosity can be derived through $L_p = 4\pi D_L^2 F_p/(1+z)$ and $L_{x,iso} = (1+z)E_{x,iso}/(T_{end} - T_{start})$, where F_p is the peak flux of flare.

3. Parameters of X-ray Flares and Their Correlations

Figure 2 shows the histogram distributions of the flare parameters. The peak times of flares range from between 100 s and 10^6 s after GRB trigger, mainly from 100 s to 1000 s, at the early time of afterglow phase. While according to Liang et al. (2010) and Yi et al. (2013), the peak time of the optical onset bump is also in the range of 100 - 1000 s statistically. Therefore the peak times of flares are nearly matching the peak times of optical afterglow onset bumps. The distributions of rise times and decay times are more symmetric. Both of them are in the range 10 to 10^6 s. The isotropic energy of the X-ray flare with redshift can be estimated from the fluence. The energy of flares mainly distributed from 10^{50} erg to 10^{52} erg, about less than two orders of magnitude compared with GRBs prompt emission. If the Gaussian function is used to fit the 0.3-10 keV isotropic energy of X-ray flares, the peak of the distribution is $10^{51.2}$ erg. Although the distribution is quite skewed and the peak of the fitting does not coincide with the peak of the energy distribution. The peak luminosity of X-ray flares mainly range from 10^{48} erg s^{-1} to 10^{50} erg s^{-1}, generally two or three orders of magnitude larger than the peak luminosity of the optical afterglow bumps. In the next paragraph, we will discuss the possible correlations among those parameters of X-ray flares.

Figure 3 demonstrates the existence of a strong correlation between the rise and decay times (the left one), i.e., $T_{decay} \propto T_{rise}$, with the slope index 0.93. Generally, the decay time is longer than the rise time, which is the general property of shocks. There is also a strong correlation between the flare duration time and the peak time. The duration times of X-ray flares range from 10 s to 10^6 s, and mainly distribute between 100 s and 1000 s. These two tight correlations suggest that longer rise times associate with longer decay times, and also indicate broader flares peak at later times.

We show some correlations among the characteristics of the X-ray flares in the following figures. The correlations and linear correlation coefficients from the Spearman pair correlation analysis are shown in Table 2. Figure 4 shows correlations between the peak luminosity and the flare time scales. These correlations clearly demonstrate that a dimmer pulse of X-ray flare tends to peak at a later time with a longer duration time. The correlation between peak luminosity and the isotropic energy (the mean luminosity) indicates that a flare with larger $E_{x,iso}$ ($L_{x,iso}$) tends to have a brighter X-ray flare peaking at earlier time.

Figure 5 shows correlations between the mean luminosity and the timescales of flares, which are transferred into the rest frame. We obtain the mean luminosity thought the isotropic energy divided by duration, i.e., $L_{x,iso} = (1+z)E_{x,iso}/(T_{end} - T_{start})$. We find that the mean luminosity is also tightly anti-correlated with the time-scales of X-ray flares. These correlations between mean luminosity and the timescales indicate that a dimmer X-ray flare peaking at a later time also with a longer duration time. Figure 6 shows the correlations between the waiting time and other parameters of flares. The waiting time is correlated with both the peak time and the duration time, which means a longer waiting time tends to peak at a later time with a longer duration time. Besides, the waiting time is anti-correlated with both the peak luminosity and the mean luminosity. From above discussions, we conclude that these correlations are consistent with each other.

4. The Frequency Distributions of Flare Parameters

The erratic X-ray flares generally supposed to be produced by the late activities of central engine, therefore X-ray flares may share a similar physical mechanism as GRB prompt emission. A lot of work has been done to investigate their physical origin. Wang & Dai (2013) studied the distributions of the energies, duration times and waiting times of solar flares and GRB X-ray flares. They found both of them have similar statistical distributions. Apart from GRBs, Wang et al. (2015) discovered that X-ray flares from the black hole systems share the similar statistical properties with solar flares, including Swift J1644+57, M87 and Sgr A*. Solar flares are driven magnetic reconnection (Lu & Hamilton 1991; Charbonneau et al. 2001; Morales & Charbonneau 2008; Aschwanden 2012). The power-law distributions of X-ray flare parameters indicate that they may be self-organized criticality (SOC) events (Bak et al. 1987, 1988) driven by magnetic reconnection. This suggests that GRB jet contains a significant fraction of Poynting flux. The ratio σ between the Poynting flux F_P and baryonic flux F_b is larger than unity, i.e., $\sigma = F_P/F_b \geq 1$ (Zhang & Yan 2011). Meanwhile the GRB prompt emission is likely powered by dissipation of magnetic field energy (Lei et al. 2013; Yi et al. 2015b; Jia et al. 2015). Recently, Uhm & Zhang (2015) also studied the steep

decay phase after the peak time of X-ray flare and found the decay slope is steeper than the standard value $\alpha = 2 + \beta$, where α and β are the decay slope of light curve and the observed spectral index, respectively. This standard value can be understood as follows. For a conical jet of GRB with an opening angle θ_j, emission from the same radius R but from different viewing latitudes $\theta\,(\theta < \theta_j)$ would reach the observer at different times, which is called curvature effect. If the emission area keeps a constant Lorentz factor Γ, there exists a simple relation $\alpha = 2 + \beta$ (i.e., Kumar & Panaitescu 2000). In the same situation, the flare decay properties demand that the emission region is undergoing significant bulk acceleration. In the following, we will study the distributions of flare parameters using a large sample.

We present the differential distributions of solar hard X-ray flares in Figure 7. Because the number of solar flares is very large, we select 11595 solar flares observed by *RHESSI* (Aschwanden 2011). We consider distribution of energy, waiting time, duration time and peak flux. The number of flares $N(E)dE$ with energy between E and $E + dE$ can be expressed by

$$N(E)dE \propto E^{-\alpha_E}\, dE \quad E < E_{max}, \tag{3}$$

where α_E is the power-law index and E_{max} is the cutoff energy. With this equation, we obtain the cumulative energy distribution

$$N(> E) = a + b[E^{1-\alpha_E} - E_{max}^{1-\alpha_E}], \tag{4}$$

where a and b are two fitting parameters. The power-law slope is $\alpha_E = 1.65 \pm 0.02$ for the differential distribution of solar flares (Aschwanden 2011). For the other three parameters of solar flares, their differential distribution can be expressed as $N(X)dX \propto X^{-\alpha_X}$, where X is corresponding to a parameter of solar flares. All distributions show power-law behavior. The indices of the waiting time, duration time and peak flux are 2.04 ± 0.03, 2.00 ± 0.05 and 1.77 ± 0.02, respectively (Aschwanden 2011). These distributions support that solar flares are SOC events driven by a magnetic reconnection process occurring in the atmosphere of the Sun. Therefore, the distributions of solar flares could be well understood within a physical framework, i.e., SOC.

We consider two groups of X-ray flares. In the first case, we consider all 468 X-ray flares. Since some of them have no detected redshift, we don't make any correction of the their time parameters. To get the differential distributions of these varieties, we separate them into 20 bins in the equal logarithmic space and then use power-law function to fit them. We apply the Markov Chain Monte Carlo (MCMC) technique to obtain the best fitting parameters and give the 95% confidential region. Besides, we also consider the cumulative distribution of the peak flux of X-ray flares in this case. We also use the fit function $N(> F) = a + b[F^{1-\alpha_F} - F_{max}^{1-\alpha_F}]$ and the MCMC method to obtain the optimal parameter and give the 95% confidential region. The fitting result of the distribution of these time parameters are shown in Figure 8.

In the second case, we only consider those X-ray flares with detected redshifts, which makes our sample only include 200 X-ray flares. In this case, we transfer the time parameters into the rest frame with $t_{rest} = t_{obs}/(1+z)$. Moreover, because all of the X-ray flares in this sub-sample have detected redshifts, we can calculate the isotropic energy through $E_{iso} = 4\pi D_L^2 S_F/(1+z)$. The energy distributions GRB X-ray flares show a flat part at the low energy regime, which could be due to incomplete sampling and some selection bias for large energy flares (Cliver et al. 2012). Therefore, in order to avoid this selection effect, we only select the distribution above the break to be fitted. Then, just same as the total sample, we use MCMC method to obtain the optimal fit parameters and the 95% confidential regions for the distributions. The results are shown in Figure 9.

From Figure 8 and Figure 9, we find that the differential distributions of the time parameters, can be well fitted with the power-law function both for the total sample and the sub-sample with detected redshifts. In Figure 8, the power-law indices of the peak times, rise times, decay times, waiting times and duration times for the total sample are -1.95 ± 0.09, -1.56 ± 0.04, -1.51 ± 0.06, -1.89 ± 0.13, and -1.56 ± 0.05, respectively. While in Figure 9, the power-law indices of the peak times, rise times, decay times, waiting times and duration times for the sub-sample with redshifts are -1.72 ± 0.11, -1.41 ± 0.04, -1.33 ± 0.08, -1.44 ± 0.05, and -1.41 ± 0.05, respectively. There are a little differences between the best-fitting parameters in the two cases. For the cumulative distribution of peak flux and isotropic energy of X-ray flares, we also obtain the power-law slopes. For the total sample, we get the optimal parameter $\alpha_F = 1.52 \pm 0.03$ for peak flux cumulative distribution. Meanwhile, for the sub-sample, we get the optimal parameter $\alpha_E = 1.32 \pm 0.07$ for isotropic energy cumulative distribution. These power-law distributions are natural predications of SOC theory (Aschwanden 2011).

Figure 10 shows the power-law distributions of solar flares and GRB X-ray flares. Although the energies of GRB X-ray flares are in the range from 10^{49} erg to 10^{53} erg, and 10^{28} erg to 10^{32} erg for solar flare energies, they show power-law distributions with different indices. These distributions can be understood in fractal-diffusive avalanche model (Aschwanden 2012). The magnetic reconnection as physical origin of solar flares is well recognized (Sweet 1958; Parker 1957; for a recent review, see Shibata & Magara 2011). For solar flares, the total magnetic energy E_B released during a reconnection process in an elementary volume L^3 with an average magnetic energy density $B^2/8\pi$ is (Shibata & Magara 2011)

$$E_B = L^3 \frac{B^2}{8\pi} \sim 3 \times 10^{30} (\frac{B}{10^2 G})^2 (\frac{L}{2 \times 10^9 cm})^3 \ \text{erg}, \tag{5}$$

which is the typical energy of solar flare. For models of GRB X-ray flares, there are several magnetic reconnection models. Dai et al. (2006) proposed that X-ray flares could be produced by differentially rotating, millisecond pulsars. The differential rotation leads to

windup of interior poloidal magnetic fields and the toroidal fields break through the stellar surface. The energy from reconnection toroidal fields with different polarity is (Dai et al. 2006; Kluzniak & Ruderman 1998)

$$E_b = \frac{E_b^2}{8\pi} V_b \sim 1.6 \times 10^{51} \frac{V_b}{V_*} \text{ erg}, \tag{6}$$

where V_b and V_* are the toroid's volume and the stellar volume, respectively. This energy is comparable to the observed one. X-ray flares of GRBs may also be powered by magnetic dissipation in a decelerating shell (Giannios 2006). The analysis by Giannios (2006) shows that the energy emitted in a single flare E_f and produced by a single reconnection event is

$$E_f \leq 5\epsilon \frac{E_{fs}}{\delta^2} \sim 1.25 \times 10^{52} (\frac{E_{fs}}{10^{53} erg}) (\frac{\delta}{2})^{-2} \text{ erg}, \tag{7}$$

where E_{fs} is the isotropic energy of the forward shock, and $\epsilon \sim 0.1$ the fraction of the Alfvén speed of the magnetic reconnection in a strongly magnetized plasma. For a constant-density medium, the typical value of δ is four (Waxman 1997). In stellar wind case, the value of δ is two (Pe'er & Waxman 2005). So the energy budgets of these models are comparable to the observed energies of X-ray flares.

5. Conclusions and Discussion

In this paper, we present a catalog of 468 bright X-ray flares of GRBs taken from the online *Swift/XRT* GRB Catalogue until March 2015, including 200 flares with redshifts. We use a smooth broken power-law function to fit the X-ray flares, and obtain the fitting parameters of X-ray flares, which are listed in Table 1. The peak times of flares range from between 100 s and 10^6 s after GRB trigger, mainly from 100 s to 1000 s. The duration times of flares also mainly distribute between 100 s and 1000 s. The 0.3-10 keV isotropic energy of X-ray flares mainly distributed from 10^{50} erg to 10^{52} erg, which is about less than two or three orders of magnitude compared with GRBs prompt emission. The 0.3-10 keV isotropic energy of X-ray flares distribution is a lognormal peaked at $10^{51.2}$ erg. We also found some tight correlations between these parameters of X-ray flares, and the best-fitting results for the correlations are shown in Table 2. Generally, these correlations clearly demonstrate that a dimmer pulse of X-ray flare tends to peak at a later time with a longer duration time.

We also study the frequency distributions of solar flares and GRB X-ray flares. In the analysis, we combine all X-ray flares from long and short GRBs. Some studies indicated that X-ray flares in long and short GRBs may have a common origin (Margutti et al. 2011; Wang & Dai 2013). The best-fitting results for the power-law distributions of these parameters are

shown in Figures 7, 8, and 9. We find there are four power-law distributions with different indices between X-ray flares and solar flares, including power-law distributions of energies, durations, peak fluxes and waiting times. These distributions could be explained by a fractal-diffusive, self-organized criticality model. Besides, we also investigate the peak times, rising times and decay times of X-ray flares, and find all of them show power-law distributions.

Interestingly, the ratio $T_{duration}/T_{peak}$ is almost constant with time in our X-ray flare sample (see right panel of Fig. 3). This result is also found by Chincarini et al. (2010). The late internal shock model can not account for this result since the arrival time is not related to the collision conditions (Kobayashi et al. 1997; Ramirez-Ruiz & Fenimore 2000). Further more, the efficiency of internal collision is typically low (Panaitescu et al. 1999; Kumar 1999; Fan & Wei 2005).

X-ray flares may also be powered by magnetic dissipation in a decelerating shell (Giannios 2006). MHD instability could be triggered in strongly magnetized ejecta during its deceleration due to interaction with the external medium. This instability can release energy through magnetic reconnection. Multiple flares are expected because of dissipation in multiple neighboring regions in the decelerating flow. This model also predicts that smooth flares are more energetic than spiky ones (Giannios 2006). Chincarini et al. (2010) compared this model with X-ray flare data, and found this model is not in contradiction with observation. However more test are needed. Another possible model for X-ray flares is the internal-collision-induced magnetic reconnection and turbulence model, which can also reproduce the properties of GRB prompt emission (Zhang & Yan 2011). In this model, internal collisions distort the ordered magnetic field lines in the ejecta. The X-ray flares can be triggered by magnetic reconnection in the distorted magnetic field. So these two models are favored from our analysis. However, much more data are required to constrain the model parameters.

Acknowledgments

We thank an anonymous referee for useful suggestions and comments. We many thank Zi-Gao Dai and Bing Zhang for valuable comments. This work is supported by the National Basic Research Program of China (973 Program, grant No. 2014CB845800) and the National Natural Science Foundation of China (grants 11422325, 11373022, 11533003 and 11163001), the Excellent Youth Foundation of Jiangsu Province (BK20140016).

REFERENCES

Abramowski, A., Acero, F., Aharonian, F., et al. 2012, ApJ, 746, 151

Aschwanden, M. J., 2011, Self-Organized Criticality in Astrophysics: The Statistics of Nonlinear Processes in the Universe, Springer-Verlag: Berlin

Aschwanden, M. J. 2012, A&A, 539, A2

Baganoff, F. K., Bautz, M. W., Brandt, W. N., et al. 2001, Nature, 413, 45

Bak, P., Tang, C., & Wiesenfeld, K. 1988, Phys. Rev. A, 38, 364

Bak, P., Tang, C., & Wiesenfeld, K. 1987, Physical Review Letters, 59, 381

Bernardini, M. G., Margutti, R., Chincarini, G., Guidorzi, C., & Mao, J. 2011, A&A, 526, A27

Burrows, D. N., Kennea, J. A., Ghisellini, G., et al. 2011, Nature, 476, 421

Burrows, D. N., Romano, P., Falcone, A., et al. 2005, Science, 309, 1833

Campana, S., Tagliaferri, G., Lazzati, D., et al. 2006, A&A, 454, 113

Chapman, S. C., Watkins, N. W., Dendy, R. O., Helander, P., & Rowlands, G. 1998, Geophys. Res. Lett., 25, 2397

Charbonneau, P., & MacGregor, K. B. 2001, ApJ, 559, 1094

Chincarini, G., Mao, J., Margutti, R., et al. 2010, MNRAS, 406, 2113

Chincarini, G., Moretti, A., Romano, P., et al. 2007, ApJ, 671, 1903

Cliver, E. W., Ling, A. G., Belov, A., & Yashiro, S. 2012, ApJ, 756, L29

Crosby, N., Vilmer, N., Lund, N., Klein, K.-L., & Sunyaev, R. 1996, Sol. Phys., 167, 333

Dai, Z. G., Wang, X. Y., Wu, X. F., & Zhang, B. 2006, Science, 311, 1127

De Young, D. S. 1991, Science, 252, 389

Evans, P. A., Beardmore, A. P., Page, K. L., et al. 2007, A&A, 469, 379

Evans, P. A., Beardmore, A. P., Page, K. L., et al. 2009, MNRAS, 397, 1177

Falcone, A. D., Burrows, D. N., Lazzati, D., et al. 2006, ApJ, 641, 1010

Falcone, A. D., Morris, D., Racusin, J., et al. 2007, ApJ, 671, 1921

Fan, Y. Z., & Wei, D. M. 2005, MNRAS, 364, L42

Giannios, D. 2006, A&A, 455, L5

Guidorzi, C., Dichiara, S., Frontera, F., et al. 2015, ApJ, 801, 57

Harko, T., Mocanu, G., & Stroia, N. 2015, Ap&SS, 357, 84

Harris, D. E., Cheung, C. C., Stawarz, Ł., Biretta, J. A., & Perlman, E. S. 2009, ApJ, 699, 305

Hou, S. J., Geng, J. J., Wang, K., et al. 2014, ApJ, 785, 113

Jia, L.-W., Uhm, Z. L., & Zhang, B. 2015, arXiv:1509.04871

King, A., O'Brien, P. T., Goad, M. R., et al. 2005, ApJ, 630, L113

Kluźniak, W., & Ruderman, M. 1998, ApJ, 505, L113

Kumar, P. 1999, ApJ, 523, L113

Kumar, P., & Panaitescu, A. 2000, ApJ, 541, L51

Kobayashi, S., Piran, T., & Sari, R. 1997, ApJ, 490, 92

Lei, W.-H., Zhang, B., & Liang, E.-W. 2013, ApJ, 765, 125

Li, L., Liang, E.-W., Tang, Q.-W., et al. 2012, ApJ, 758, 27

Liang, E.-W., Zhang, B., O'Brien, P. T., et al. 2006, ApJ, 646, 351

Liang, E.-W., Yi, S.-X., Zhang, J., et al. 2010, ApJ, 725, 2209

Lu, E. T., & Hamilton, R. J. 1991, ApJ, 380, L89

Margutti, M., et al. 2011, MNRAS, 417, 2144

Meier, D. L., Koide, S., & Uchida, Y. 2001, Science, 291, 84

Mirabel, I. F., & Rodríguez, L. F. 1999, ARA&A, 37, 409

Morales, L., & Charbonneau, P. 2008, ApJ, 682, 654

Negoro, H., Kitamoto, S., Takeuchi, M., & Mineshige, S. 1995, ApJ, 452, L49

Neilsen, J., Nowak, M. A., Gammie, C., et al. 2013, ApJ, 774, 42

Nousek, J. A., Kouveliotou, C., Grupe, D., et al. 2006, ApJ, 642, 389

Omori, F. 1895, J. Coll. Sci. Imper. Univ. Tokyo, 7, 111

Parker, E. N. 1957, Physical Review, 107, 830

Panaitescu, A., Spada, M., & Mészáros, P. 1999, ApJ, 522, L105

Pe'er, A., & Waxman, E. 2005, ApJ, 628, 857

Perna, R., Armitage, P. J., & Zhang, B. 2006, ApJ, 636, L29

Proga, D., & Zhang, B. 2006, MNRAS, 370, L61

Ramirez-Ruiz, E., & Fenimore, E. E. 2000, ApJ, 539, 712

Romano, P., Moretti, A., Banat, P. L., et al. 2006, A&A, 450, 59

Shibata, K., & Magara, T. 2011, Living Reviews in Solar Physics, 8, 6

Sweet, P. A. 1958, Electromagnetic Phenomena in Cosmical Physics, 6, 123

Swenson, C. A., & Roming, P. W. A. 2014, ApJ, 788, 30

Uhm, Z. L., & Zhang, B. 2015, arXiv:1509.03296

Waxman, E., 1997, ApJ, 491, L19

Wang, F. Y., & Dai, Z. G. 2013, Nature Physics, 9, 465

Wang, F. Y., Dai, Z. G., Yi, S. X., & Xi, S. Q. 2015, ApJS, 216, 8

Wheatland, M. S., Sturrock, P. A., & McTiernan, J. M. 1998, ApJ, 509, 448

Wu, X.-F., Hou, S.-J., & Lei, W.-H. 2013, ApJ, 767, L36

Yi, S.-X., Wu, X.-F., & Dai, Z.-G. 2013, ApJ, 776, 120

Yi, S.-X., Wu, X.-F., Wang, F.-Y., & Dai, Z.-G. 2015a, ApJ, 807, 92

Yi, S. X., Lei, W. H., Zhang, B., Dai, Z. G., Wu, X. F., & Liang, E. W. 2015b, submitted

Zhang, B., Fan, Y. Z., Dyks, J., et al. 2006, ApJ, 642, 354

Zhang, B., & Yan, H. 2011, ApJ, 726, 90

Zhang, S. N. 2007, Highlights of Astronomy, 14, 41

This preprint was prepared with the AAS LaTeX macros v5.2.

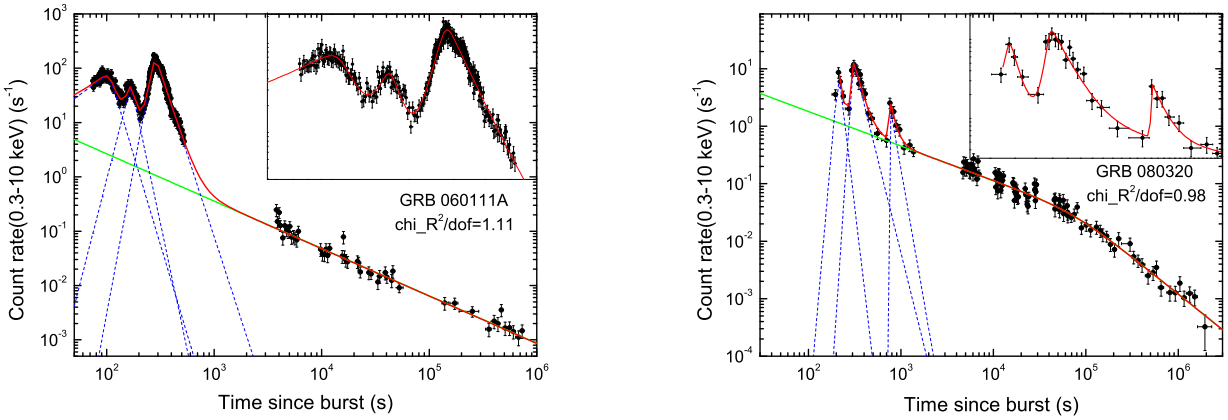

Fig. 1.— Best fitting for the X-ray flares of GRB 060111A and GRB 080320. The blue-dash lines show the best fitting for individual flares, and the green line shows the underlying continuum. The red line shows the total best fitting. Inset: the detail of flare fittings.

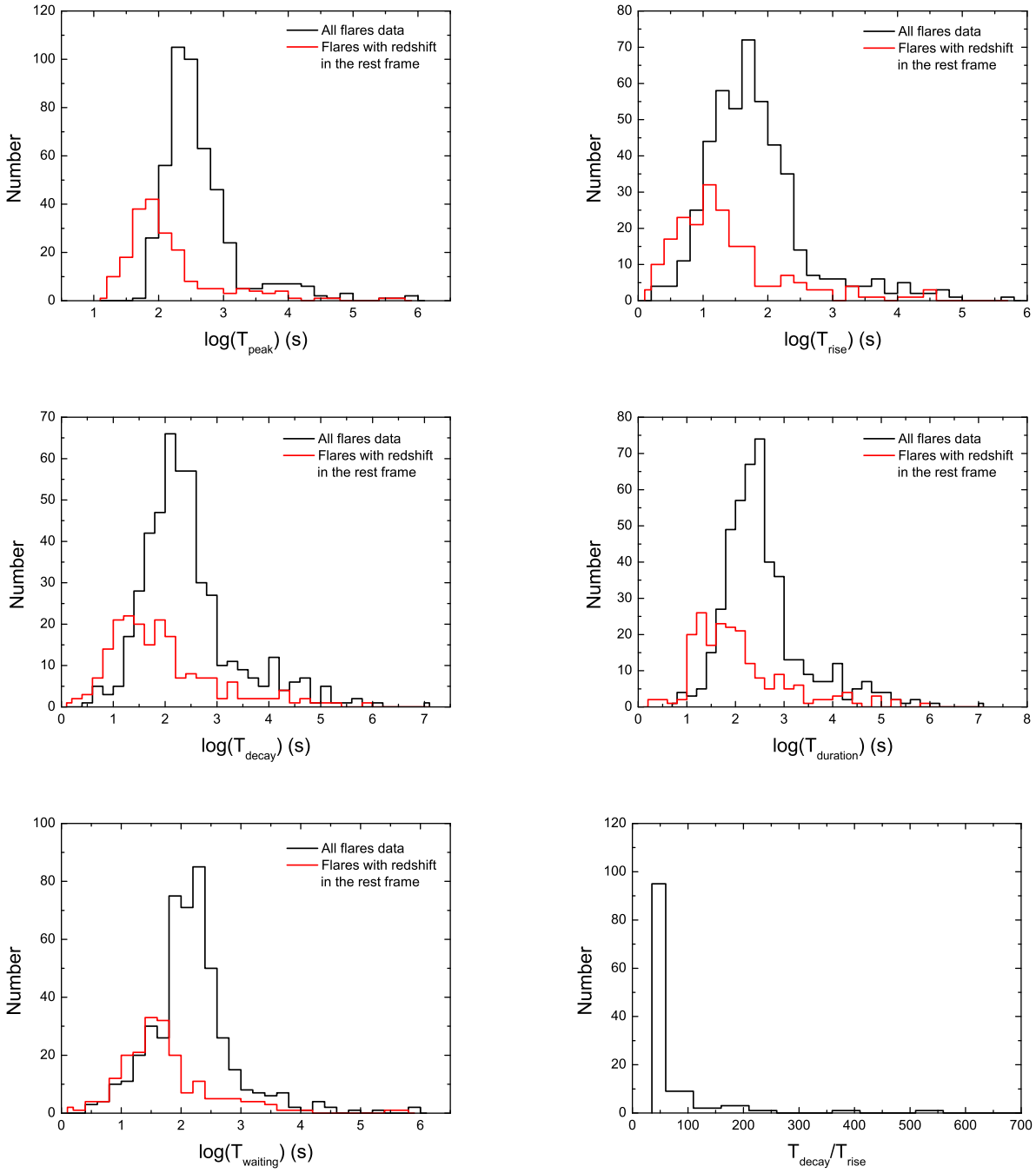

Fig. 2.— The histogram distributions of X-ray flare parameters. For the observed time parameters, the black line is corresponding to the fitting results of all the flare sample. While the red line represent the flares with reshifts, and the parameters have been transferred to the source frame. The mean value is 24.64 for T_{decay}/T_{rise}. The blue line shows the best lognormal fit of energy.

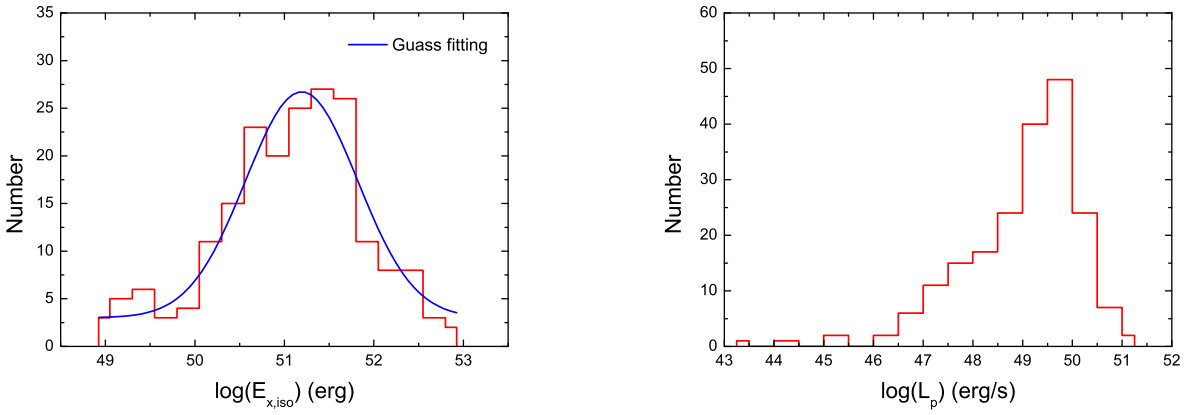

Fig. 2— Continued

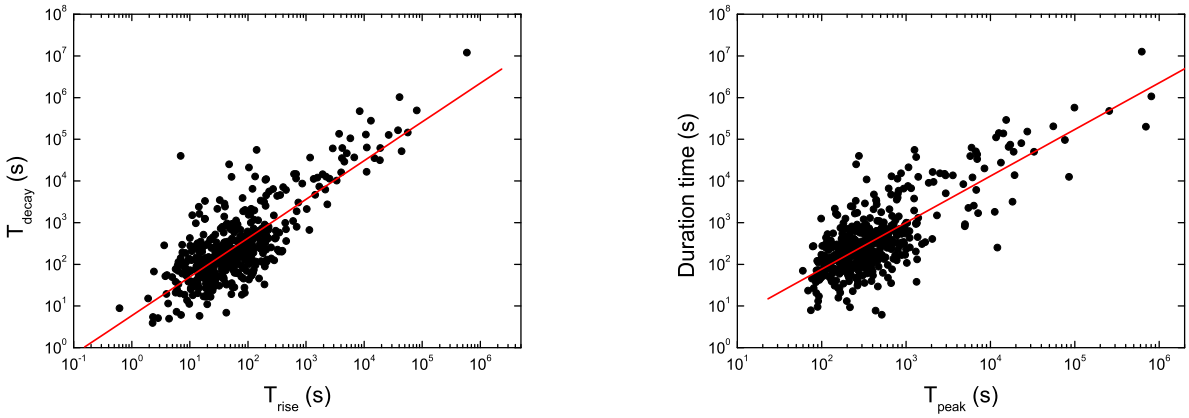

Fig. 3.— The correlations of time-scales of GRB X-ray flares. Left panel: the rise time is correlated with the decay time. Right panel: the duration is correlated with peak time. The red line is the best fitting. The best fitting results are shown in Table 2.

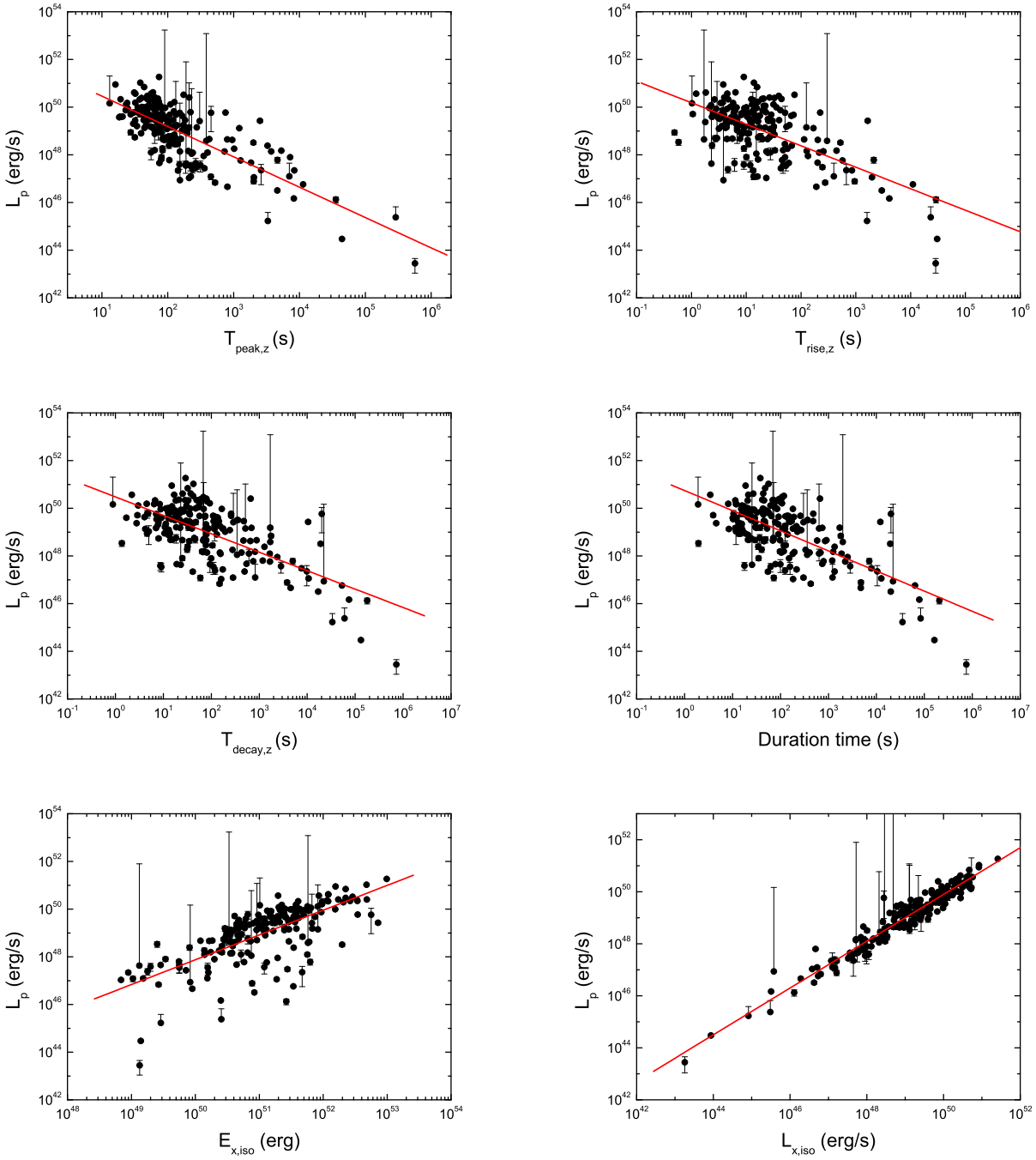

Fig. 4.— The correlations between peak luminosity and other parameters of GRB X-ray flares. The red line is the best fitting. The times are transferred into the source frame. The best fitting results are listed in Table 2.

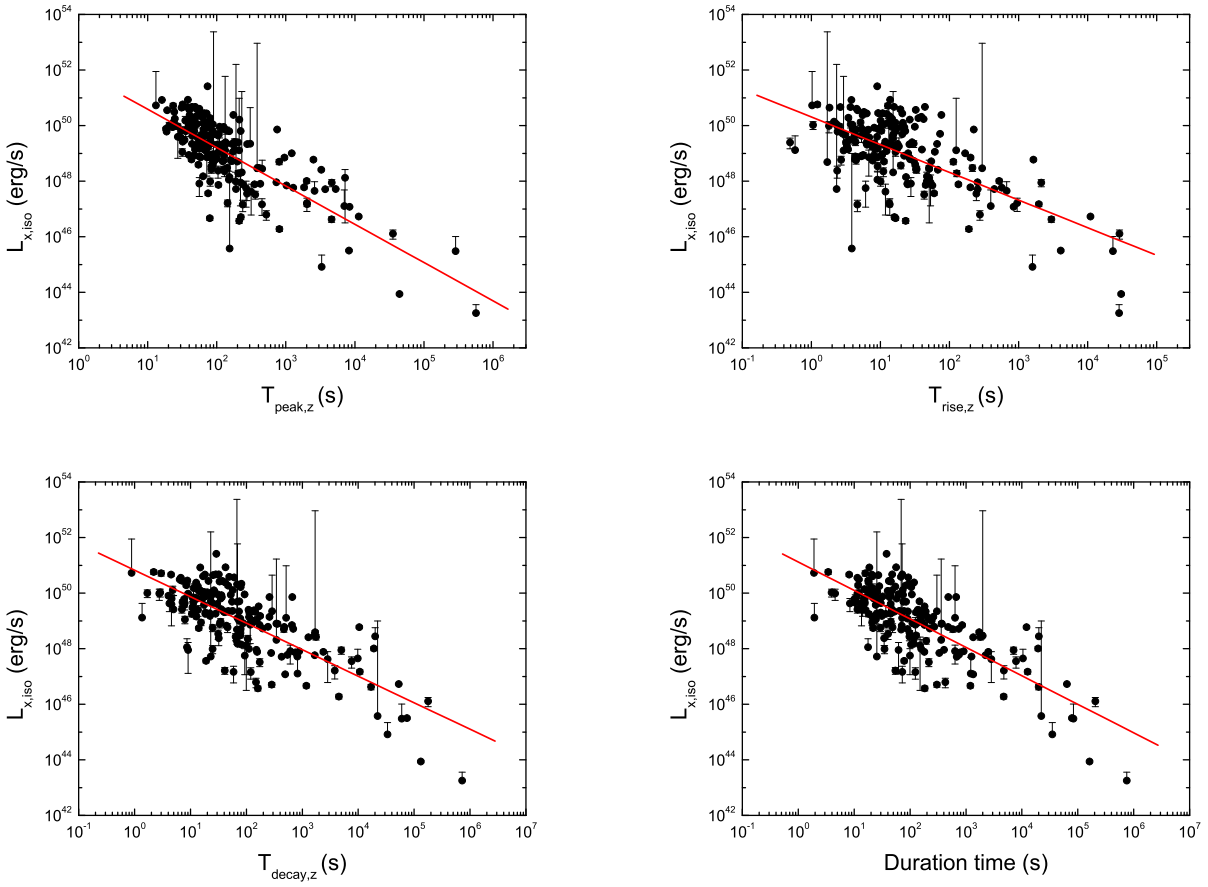

Fig. 5.— The correlations between mean luminosity and time scales of GRB X-ray flares. Red lines are the best fittings. The best fitting results can be seen in Table 2.

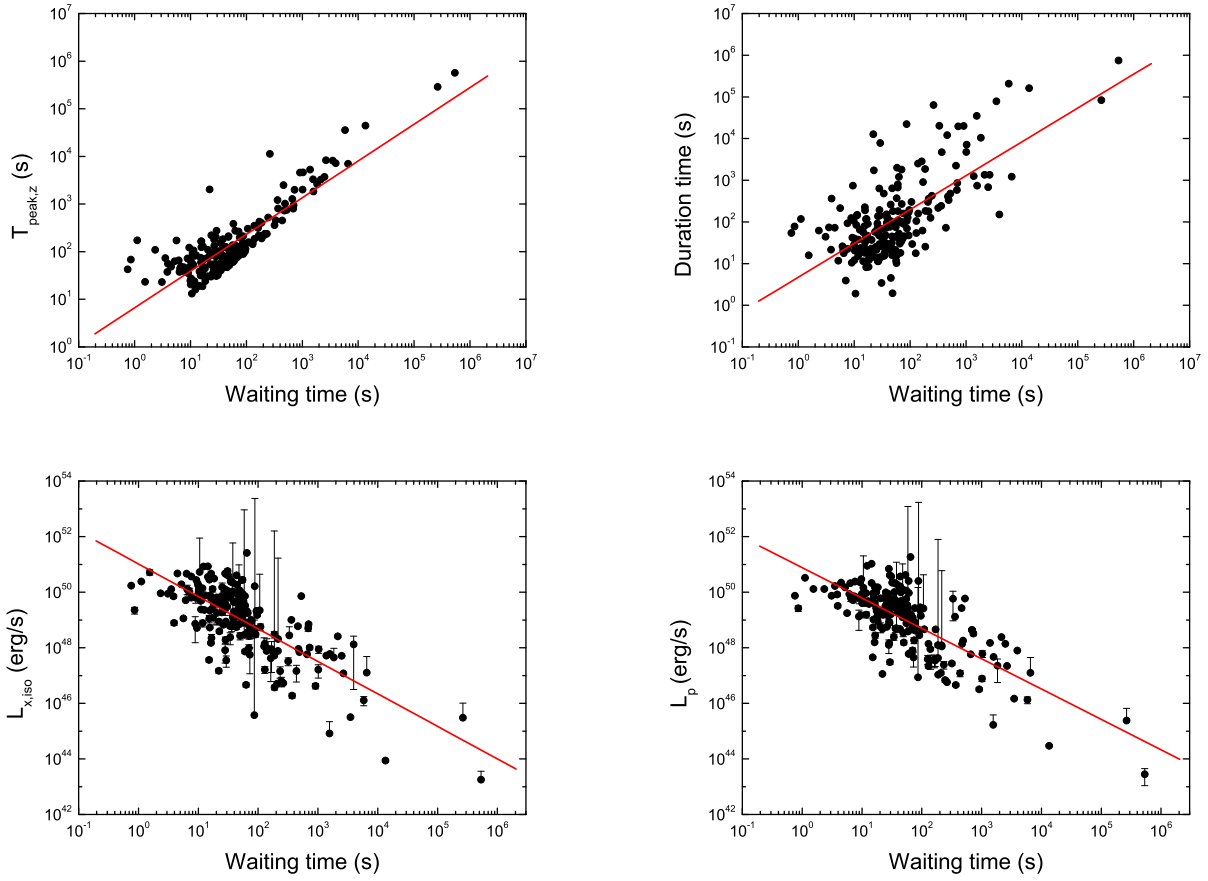

Fig. 6.— The correlations between waiting time and other parameters of GRB X-ray flares. The symbols have the same meanings as in Figure 4. The best fitting results can be seen in Table 2.

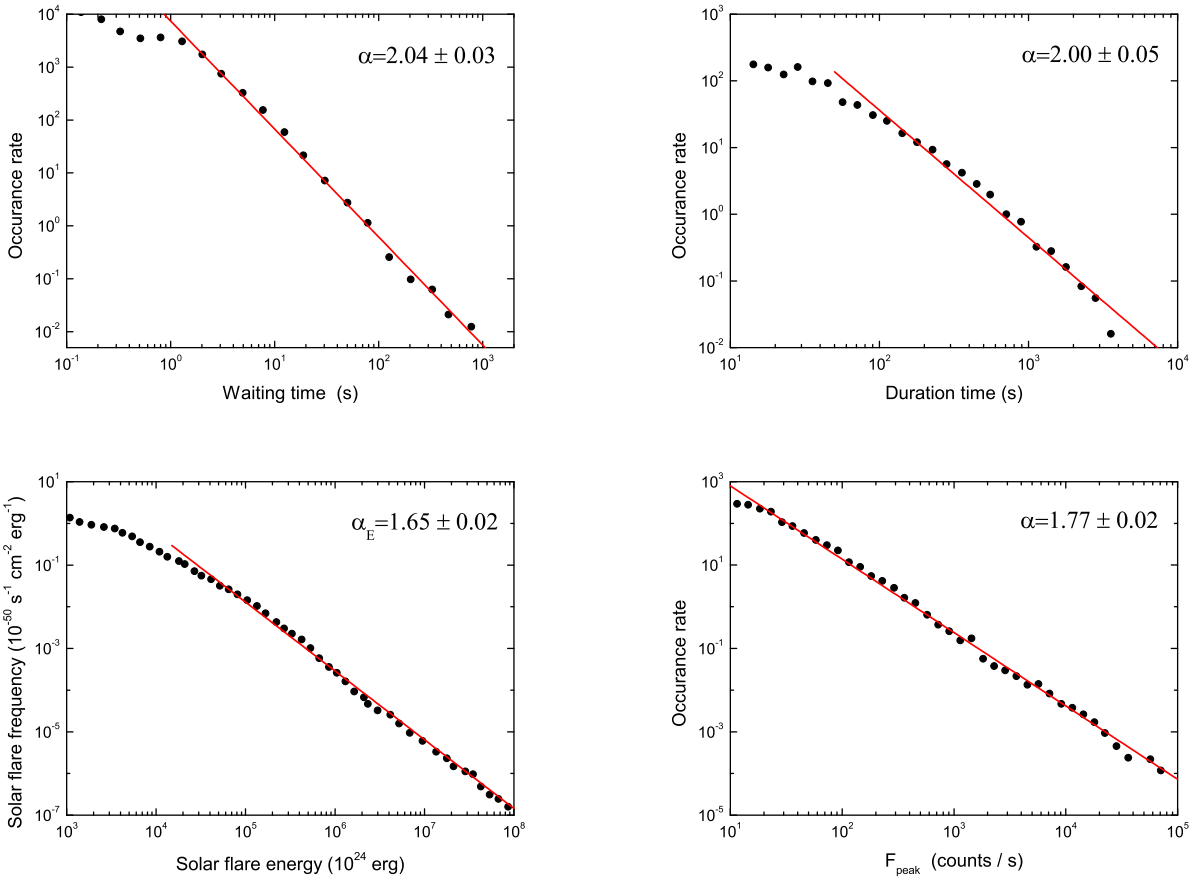

Fig. 7.— The cumulative distributions of solar hard X-ray flares. 11595 solar flares from *RHESSI* during 2002-2007 are shown as black dots (Aschwanden 2011). The best-fit α for the power-law distributions of waiting time, duration time, energy and peak flux are 2.04 ± 0.03, 2.00 ± 0.05, 1.65 ± 0.02, and 1.77 ± 0.02, respectively.

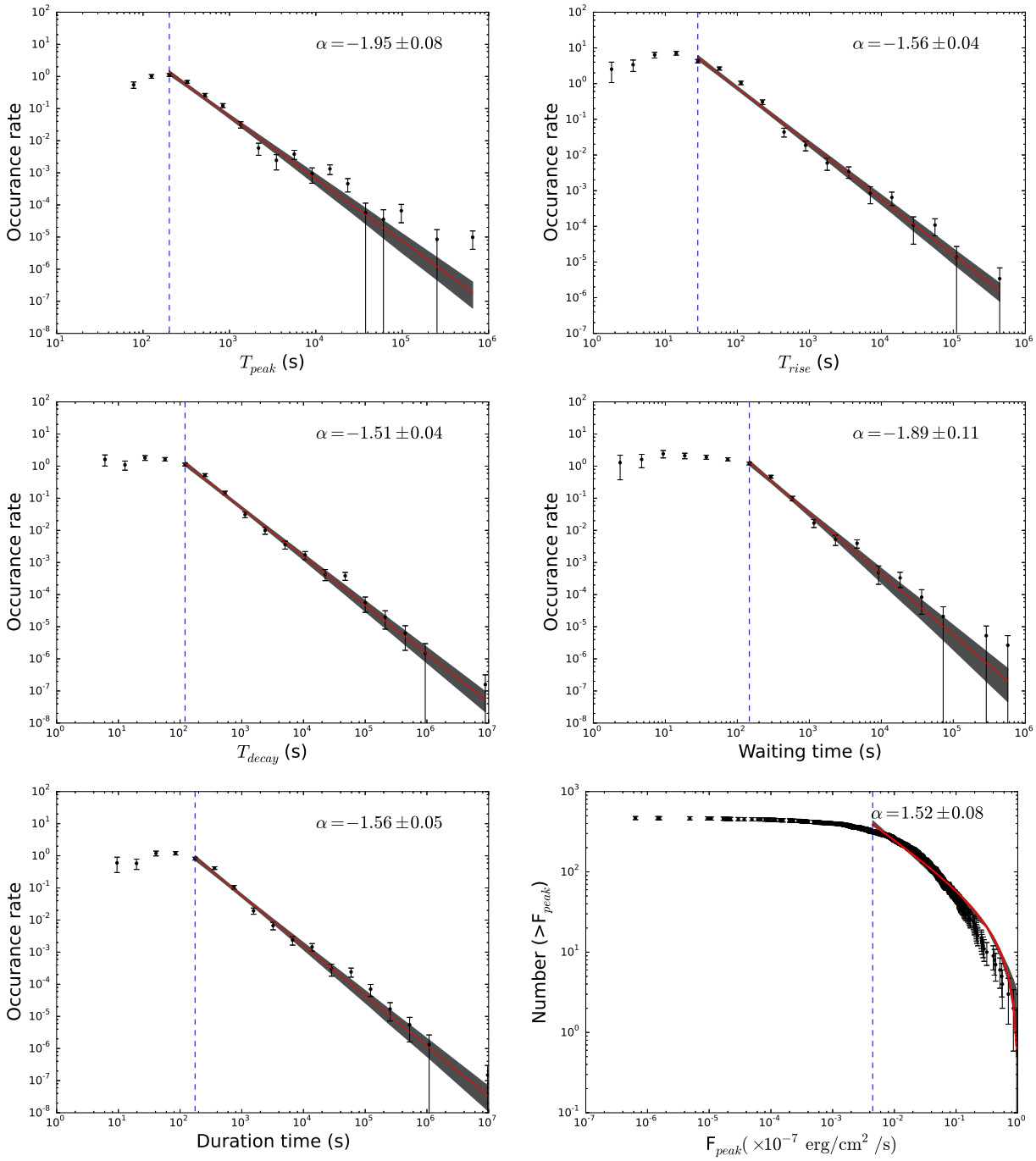

Fig. 8.— The distributions of GRB X-ray flares. The best-fit indices for the differential distributions of peak time, rise time, decay time, waiting time and duration time of X-ray flares are -1.95 ± 0.08, -1.56 ± 0.04, -1.51 ± 0.04, -1.89 ± 0.11 and -1.56 ± 0.05 respectively. The gray region shows the 95% confidence level. The optimal parameter of the cumulative distribution for X-ray flare peak flux is $\alpha = 1.52 \pm 0.08$.

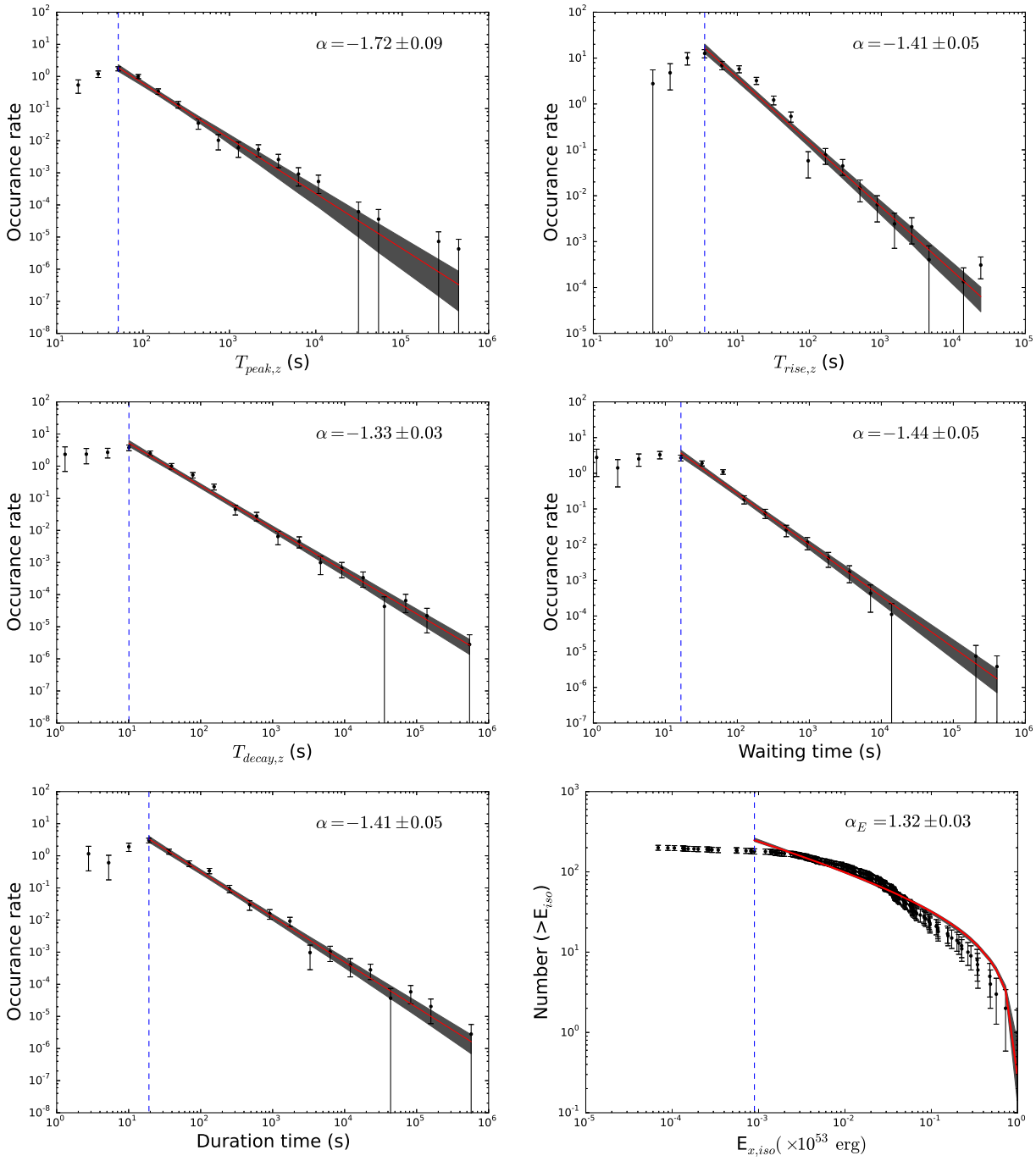

Fig. 9.— The distributions of GRB X-ray flares with redshift. 200 GRB flares are used. The observed times of the flares are transferred into the source frame. The best-fit indices for the frequency distributions of peak time, rise time, decay time, waiting time and duration time of X-ray flares are -1.72 ± 0.09, -1.41 ± 0.05, -1.33 ± 0.03, -1.44 ± 0.05 and -1.41 ± 0.05 respectively. The gray region shows the 95% confidence level. The optimal parameter for the cumulative distribution of isotropic energy of X-ray flares is $\alpha_E = 1.32 \pm 0.03$.

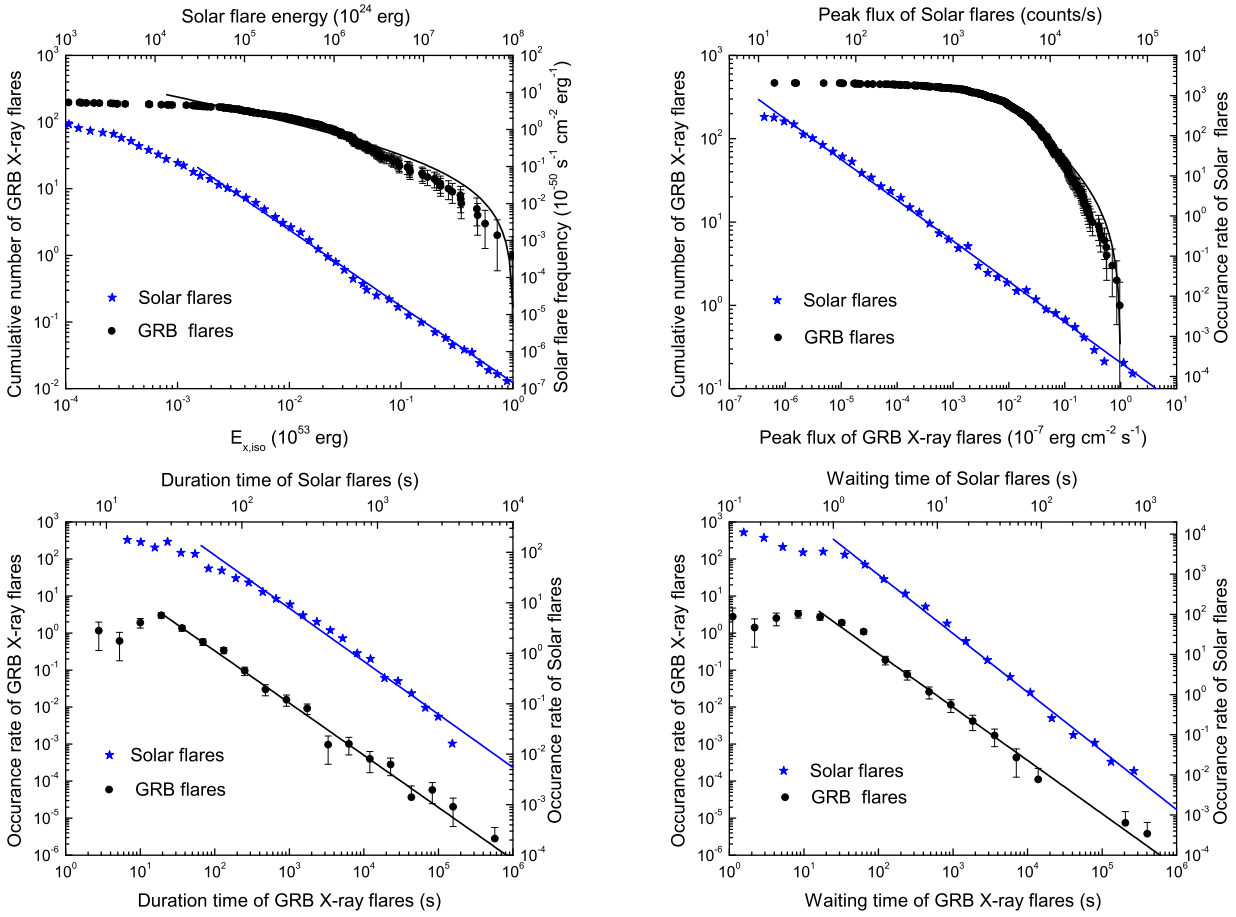
Solar flare energy (10^{24} erg)
Cumulative number of GRB X-ray flares
Solar flare frequency (10^{-50} s^{-1} cm^{-2} erg^{-1})
Solar flares
GRB flares
$E_{x,iso}$ (10^{53} erg)
Peak flux of Solar flares (counts/s)
Occurance rate of Solar flares
Peak flux of GRB X-ray flares (10^{-7} erg cm^{-2} s^{-1})
Duration time of Solar flares (s)
Occurance rate of GRB X-ray flares
Occurance rate of Solar flares
Duration time of GRB X-ray flares (s)
Waiting time of Solar flares (s)
Waiting time of GRB X-ray flares (s)

Fig. 10.— The comparison between solar flares (blue stars) and GRB X-ray flares (black dots). In the up two panels, the distributions are differential distribution and cumulative distribution for solar flares and GRB X-ray flares, respectively. The best-fitting indices can be found in Figures 7, 8 and 9.

Table 1. Fitting Results of X-ray Flares.

GRB	z	T_{start} (s)	T_{peak} (s)	T_{end} (s)	F_p (10^{-10}erg cm^{-2} s^{-1})	S_F (10^{-8}erg cm^{-2})	L_p (10^{48}erg s^{-1})	$E_{x,iso}$ (10^{50}erg)
050406	2.44	55.8 ± 15.0	218.1 ± 7.3	457.6 ± 24.7	1.19 ± 0.11	1.31 ± 0.13	1.58 ± 0.15	1.74 ± 0.17
050502B	–	414.2 ± 7.4	713.7 ± 5.3	1352.2 ± 22.2	33.31 ± 0.46	80.86 ± 1.15	–	–
050502B	–	32171.8 ± 8920.4	76347.6 ± 3768.3	128229.1 ± 7230.3	0.01 ± 0.00	5.64 ± 1.06	–	–
050607	–	267.1 ± 6.1	309.7 ± 2.5	562.5 ± 15.1	12.37 ± 0.95	7.61 ± 0.65	–	–
050712	–	212.2 ± 5.0	216.6 ± 3.4	221.5 ± 3.5	2.82 ± 0.90	0.23 ± 0.29	–	–
050712	–	245.4 ± 11.1	265.3 ± 4.6	276.3 ± 6.2	4.12 ± 0.71	0.98 ± 0.59	–	–
050712	–	468.7 ± 9256.0	475.6 ± 274.0	617.0 ± 317.0	3.87 ± 26.12	1.65 ± 13.70	–	–
050712	–	797.1 ± 142.3	963.5 ± 74.9	1518.1 ± 314.3	0.49 ± 0.13	1.63 ± 0.71	–	–
050713A	–	100.7 ± 0.7	109.2 ± 0.3	190.0 ± 1.7	93.67 ± 3.38	18.92 ± 0.82	–	–
050713A	–	158.3 ± 2.2	167.6 ± 0.9	233.4 ± 5.4	12.50 ± 0.85	3.51 ± 0.35	–	–
050714B	–	280.4 ± 17.3	382.9 ± 7.7	764.7 ± 38.8	2.16 ± 0.25	2.23 ± 0.28	–	–
050716	–	27.6 ± 162.8	112.4 ± 35.4	466.0 ± 82.1	24.69 ± 8.23	36.27 ± 15.79	–	–
050716	–	161.9 ± 1.8	165.5 ± 0.8	450.4 ± 184.8	12.53 ± 1.57	9.47 ± 2.45	–	–
050716	–	346.1 ± 11.0	380.5 ± 5.3	489.0 ± 19.2	3.77 ± 0.40	2.71 ± 0.51	–	–
050724	0.257	236.3 ± 13.4	265.4 ± 3.8	467.0 ± 4.8	6.81 ± 0.59	4.39 ± 0.88	0.11 ± 0.01	0.07 ± 0.01
050724	0.257	17195.3 ± 4601.0	55578.9 ± 3054.4	220871.8 ± 12473.6	0.02 ± 0.00	8.95 ± 0.93	2.97E-4 ± 2.73E-5	0.14 ± 0.01
050726	–	156.9 ± 17.0	162.6 ± 6.2	183.5 ± 16.3	1.82 ± 1.37	0.20 ± 0.20	–	–
050726	–	251.6 ± 5.3	266.0 ± 4.5	293.2 ± 7.0	2.83 ± 0.29	0.95 ± 0.35	–	–
050730	3.97	224.7 ± 4.2	233.7 ± 2.9	247.4 ± 4.2	8.04 ± 0.86	1.49 ± 0.66	23.78 ± 2.55	4.42 ± 1.94
050730	3.97	378.2 ± 7.1	433.9 ± 3.3	506.9 ± 8.5	11.70 ± 0.51	9.71 ± 1.11	34.58 ± 1.51	28.70 ± 3.27
050730	3.97	660.9 ± 5.8	682.6 ± 4.9	736.8 ± 11.3	5.85 ± 0.49	3.55 ± 1.03	17.30 ± 1.45	10.50 ± 3.04
050803	0.422	348.5 ± 152.4	741.3 ± 44.7	953.3 ± 96.4	1.56 ± 0.27	6.08 ± 2.27	0.07 ± 0.01	0.27 ± 0.10
050803	0.422	873.8 ± 179.2	1144.8 ± 54.9	7571.7 ± 765.4	1.05 ± 0.13	20.41 ± 3.93	0.05 ± 0.01	0.89 ± 0.17
050803	0.422	5860.2 ± 968.5	11659.6 ± 755.3	117317.9 ± 1485.8	0.33 ± 0.02	57.08 ± 5.41	0.01 ± 9.93E-4	2.50 ± 0.24
050803	0.422	765783.8 ± 25387.5	806459.5 ± 1199.3	1.8E6 ± 509312.6	6.38E-4 ± 3.88E-4	3.07 ± 3.10	2.8E-5 ± 1.7E-5	0.14 ± 0.14
050820A	2.612	217.2 ± 0.7	231.5 ± 0.3	2631.9 ± 1154.3	169.48 ± 5.21	323.21 ± 19.95	252.69 ± 7.77	482.00 ± 29.70
050822	–	212.3 ± 7.9	235.7 ± 3.8	482.2 ± 8.1	4.90 ± 0.45	2.95 ± 0.41	–	–
050822	–	315.1 ± 11.6	447.6 ± 2.5	949.6 ± 24.1	11.49 ± 0.41	12.89 ± 0.48	–	–
050904	6.1	389.0 ± 13.2	465.5 ± 5.4	515.7 ± 7.6	10.05 ± 0.76	8.75 ± 1.65	57.04 ± 4.31	49.70 ± 9.35
050904	6.1	5335.1 ± 199.8	6772.2 ± 111.4	11419.2 ± 1209.2	0.75 ± 0.10	10.67 ± 1.47	4.25 ± 0.54	60.60 ± 8.35
050904	6.1	10487.7 ± 630.6	14206.7 ± 264.1	149183.3 ± 9765.1	0.57 ± 0.09	34.83 ± 5.97	3.23 ± 0.52	198.00 ± 33.90
050904	6.1	17775.0 ± 9180.9	32882.6 ± 1050.8	68190.1 ± 6920.3	0.11 ± 0.03	11.01 ± 3.12	0.61 ± 0.17	62.50 ± 17.70
050908	3.35	382.8 ± 8.3E6	390.2 ± 2.9E6	683.8 ± 4.4E6	1.98 ± 75666.73	1.49 ± 72460.91	4.46 ± 170550.38	3.36 ± 163000.00
050915A	2.5273	53.6 ± 32.3	111.9 ± 3.5	140.0 ± 6.5	3.85 ± 0.55	1.96 ± 0.59	5.42 ± 0.77	2.76 ± 0.84
050915A	2.5273	497.7 ± 21.7	529.6 ± 0	560.1 ± 25.9	0.28 ± 0.10	0.14 ± 0.14	0.39 ± 0.14	0.20 ± 0.20
050916	–	483.4 ± 2554.7	934.2 ± 1907.5	7015.6 ± 14872.3	0.14 ± 0.30	2.72 ± 9.70	–	–
050916	–	16767.3 ± 264.4	19310.3 ± 191.9	30612.3 ± 1861.9	0.38 ± 0.09	10.63 ± 2.76	–	–
050922B	–	222.7 ± 32.1	372.6 ± 3.0	1510.7 ± 177.7	13.85 ± 0.46	18.15 ± 0.64	–	–
050922B	–	480.8 ± 9.7	499.4 ± 1.9	641.0 ± 48.2	3.55 ± 0.64	0.98 ± 0.20	–	–
050922B	–	382.4 ± 25.5	819.4 ± 6.9	1805.8 ± 78.5	22.31 ± 1.51	44.45 ± 3.01	–	–
051117A	–	23.7 ± 21.2	136.6 ± 7.8	574.7 ± 50.7	58.02 ± 4.77	98.78 ± 10.22	–	–
051117A	–	242.7 ± 34.8	357.2 ± 17.1	719.1 ± 387.1	16.48 ± 2.64	33.54 ± 11.05	–	–
051117A	–	403.6 ± 17.3	439.9 ± 5.0	721.2 ± 290.0	9.82 ± 4.13	15.06 ± 12.22	–	–
051117A	–	584.7 ± 7.6	604.7 ± 4.7	680.9 ± 23.4	5.75 ± 0.68	3.49 ± 1.09	–	–
051117A	–	827.8 ± 19.5	945.2 ± 9.2	1145.3 ± 99.1	9.60 ± 1.23	15.77 ± 3.80	–	–
051117A	–	969.5 ± 53.7	1107.6 ± 7.7	1223.5 ± 30.8	9.10 ± 1.58	12.38 ± 3.54	–	–
051117A	–	1252.0 ± 5.0	1318.0 ± 1.7	2224.0 ± 71.7	21.08 ± 0.57	66.99 ± 3.29	–	–
060111A	–	23.7 ± 9.8	99.2 ± 2.3	193.4 ± 9.8	24.85 ± 1.44	16.98 ± 1.39	–	–
060111A	–	113.8 ± 11.4	167.8 ± 2.1	252.1 ± 9.9	14.29 ± 0.77	6.60 ± 0.48	–	–
060111A	–	180.5 ± 3.3	283.8 ± 0.9	752.0 ± 7.6	50.68 ± 0.74	48.27 ± 0.74	–	–

Table 1—Continued

GRB	z	T_{start} (s)	T_{peak} (s)	T_{end} (s)	F_p (10^{-10}erg cm^{-2} s^{-1})	S_F (10^{-8}erg cm^{-2})	L_p (10^{48}erg s^{-1})	$E_{x,iso}$ (10^{50}erg)
060115	3.53	354.5 ± 22.1	402.6 ± 13.1	559.7 ± 21.9	1.71 ± 0.29	1.71 ± 0.48	4.20 ± 0.72	4.20 ± 1.18
060124	2.3	318.7 ± 6.2	376.5 ± 3.3	958.9 ± 128.2	11.76 ± 0.84	24.33 ± 3.18	14.09 ± 1.01	29.20 ± 3.81
060124	2.3	322.3 ± 4.9	573.5 ± 0.7	711.6 ± 0.9	274.78 ± 7.05	239.85 ± 6.49	329.26 ± 8.45	287.00 ± 7.78
060124	2.3	611.2 ± 2.6	698.7 ± 0.8	958.9 ± 6.8	211.62 ± 4.97	143.36 ± 3.55	253.57 ± 5.95	172.00 ± 4.25
060124	2.3	961.7 ± 238.7	1005.3 ± 249.3	1959.1 ± 157424.4	21.75 ± 331.20	55.66 ± 1069.84	26.06 ± 396.86	66.70 ± 1280.00
060204B	–	81.4 ± 5.0	119.2 ± 0.7	163.7 ± 2.2	55.09 ± 2.28	15.48 ± 0.81	–	–
060204B	–	296.8 ± 3.4	318.6 ± 1.3	398.6 ± 6.2	10.04 ± 0.54	4.01 ± 0.31	–	–
060210	3.91	171.6 ± 2.2	198.7 ± 1.0	260.8 ± 3.0	35.38 ± 1.11	14.94 ± 0.80	102.13 ± 3.21	43.10 ± 2.30
060210	3.91	352.8 ± 2.1	372.2 ± 1.2	471.7 ± 6.5	16.51 ± 0.67	8.97 ± 0.63	47.66 ± 1.94	25.90 ± 1.80
060223A	4.41	1165.4 ± 457605.9	1248.0 ± 304569.7	3114.4 ± 759035.4	0.32 ± 170.05	2.15 ± 1737.24	1.12 ± 592.52	7.50 ± 6050.00
060312	–	69.3 ± 6.5	79.8 ± 2.6	344.2 ± 21.8	9.28 ± 2.56	3.48 ± 1.19	–	–
060312	–	82.2 ± 4.4	98.3 ± 1.2	155.4 ± 11.6	22.03 ± 2.90	3.29 ± 0.47	–	–
060312	–	103.4 ± 1.4	109.6 ± 0.2	204.0 ± 11.8	36.98 ± 2.90	4.76 ± 0.43	–	–
060312	–	130.7 ± 20.4	145.8 ± 4.3	285.5 ± 138.5	1.57 ± 0.59	0.59 ± 0.27	–	–
060312	–	398.6 ± 63.5	562.0 ± 30.1	910.4 ± 223.3	0.32 ± 0.06	0.69 ± 0.21	–	–
060413	–	501.5 ± 58.4	675.1 ± 28.5	1278.8 ± 107.6	4.78 ± 0.67	11.27 ± 2.05	–	–
060413	–	631.7 ± 1517.1	2955.4 ± 792.6	5689.4 ± 1544.0	1.24 ± 0.91	35.68 ± 33.00	–	–
060413	–	1350.6 ± 464.3	18836.6 ± 721.1	50386.6 ± 2435.0	0.30 ± 0.02	78.09 ± 78.09	–	–
060418	1.49	123.6 ± 0.6	129.3 ± 0.3	167.2 ± 1.0	218.49 ± 8.16	36.77 ± 1.92	119.58 ± 4.47	20.10 ± 1.05
060510B	4.9	225.1 ± 13.6	305.1 ± 2.5	786.1 ± 3.5	47.35 ± 1.65	50.72 ± 4.22	193.90 ± 6.75	208.00 ± 17.30
060510B	4.9	507.2 ± 6628.5	1244.7 ± 16266.6	4277.1 ± 73749.4	3.46 ± 250.01	20.23 ± 1469.79	14.16 ± 1023.81	82.80 ± 6020.00
060512	0.4428	187.1 ± 7.0	206.5 ± 4.2	265.7 ± 11.7	4.55 ± 0.76	1.84 ± 0.49	0.22 ± 0.04	0.09 ± 0.02
060522	5.11	112.4 ± 85.3	167.1 ± 7.8	195.0 ± 9.6	2.02 ± 0.48	1.22 ± 1.01	8.79 ± 2.09	5.32 ± 4.42
060526	3.21	224.9 ± 1.2	251.6 ± 0.4	408.0 ± 17.1	198.75 ± 7.93	56.78 ± 2.47	417.86 ± 16.67	119.00 ± 5.20
060526	3.21	239.8 ± 11.3	309.1 ± 1.2	549.6 ± 5.2	78.96 ± 4.09	44.89 ± 2.43	166.02 ± 8.60	94.40 ± 5.12
060526	3.21	4498.3 ± 3353.3	8507.2 ± 2967.6	24543.5 ± 8402.2	0.04 ± 0.01	3.67 ± 1.83	0.08 ± 0.02	7.71 ± 3.85
060602B	–	38.1 ± 53.2	182.0 ± 35.2	736.6 ± 268.3	1.84 ± 0.38	4.94 ± 1.54	–	–
060602B	–	2342.3 ± 109005.8	13332.3 ± 465705.3	29890.0 ± 2.9E6	0.02 ± 0.32	2.75 ± 45.96	–	–
060602B	–	35910.0 ± 2E8	622048.1 ± 2.5E9	1.3E7 ± 5.1E10	0.00 ± 3.39	49.59 ± 233536.06	–	–
060604	2.1357	82.0 ± 3.7	137.6 ± 0.8	369.4 ± 12.6	41.47 ± 1.15	19.12 ± 0.56	43.65 ± 1.21	20.10 ± 0.59
060604	2.1357	159.6 ± 1.9	169.9 ± 0.4	239.1 ± 7.5	30.56 ± 1.87	4.49 ± 0.31	32.16 ± 1.97	4.73 ± 0.33
060607A	3.082	41.1 ± 24.7	83.7 ± 0.7	90.6 ± 0.7	20.48 ± 2.58	6.12 ± 1.89	40.28 ± 5.08	12.00 ± 3.72
060607A	3.082	89.2 ± 1.1	97.9 ± 0.5	151.3 ± 5.4	47.29 ± 2.19	10.66 ± 0.79	92.99 ± 4.31	21.00 ± 1.56
060607A	3.082	163.3 ± 8.2	180.4 ± 4.7	197.5 ± 9.0	6.85 ± 0.85	1.83 ± 0.91	13.46 ± 1.68	3.59 ± 1.79
060607A	3.082	205.0 ± 4.4	260.0 ± 1.3	367.8 ± 6.1	38.02 ± 0.94	24.56 ± 0.96	74.76 ± 1.84	48.30 ± 1.88
060707	3.43	620.4 ± 372.2	828.2 ± 143.5	1320.8 ± 220.6	0.15 ± 0.08	0.67 ± 0.76	0.35 ± 0.18	1.56 ± 1.79
060707	3.43	1339.2 ± 380.1	1391.6 ± 2.5	13951.9 ± 5977.2	0.16 ± 0.08	5.11 ± 4.37	0.37 ± 0.18	12.00 ± 10.20
060714	2.71	75.6 ± 22.1	113.8 ± 3.4	161.2 ± 51.0	37.97 ± 5.69	9.40 ± 1.60	60.26 ± 9.03	14.90 ± 2.53
060714	2.71	109.3 ± 15.5	131.2 ± 1.1	148.3 ± 1.2	37.27 ± 13.10	4.18 ± 1.55	59.14 ± 20.78	6.63 ± 2.45
060714	2.71	123.6 ± 6.4	140.0 ± 0.7	203.9 ± 11.3	52.03 ± 7.34	9.62 ± 1.50	82.56 ± 11.65	15.30 ± 2.38
060714	2.71	152.0 ± 3.1	175.2 ± 0.6	235.7 ± 3.4	44.02 ± 1.99	9.11 ± 0.46	69.86 ± 3.15	14.50 ± 0.72
060719	1.532	178.1 ± 10.6	203.6 ± 7.2	266.6 ± 21.2	1.40 ± 0.30	0.59 ± 0.19	0.81 ± 0.17	0.34 ± 0.11
060804	–	513.3 ± 26.7	515.6 ± 24.7	519.5 ± 26.4	0.59 ± 0.16	0.04 ± 0.46	–	–
060904A	–	258.6 ± 7.0	313.5 ± 3.5	487.8 ± 8.2	6.27 ± 0.36	5.25 ± 0.43	–	–
060904A	–	645.0 ± 9.7	679.1 ± 4.5	928.1 ± 41.5	1.72 ± 0.16	1.93 ± 0.29	–	–
060904B	0.703	130.0 ± 0.8	172.7 ± 0.7	399.7 ± 7.3	214.67 ± 3.16	126.94 ± 7.83	26.90 ± 0.40	15.90 ± 0.98
060926	3.208	253.7 ± 62.5	443.3 ± 26.1	3591.1 ± 360.6	0.29 ± 0.03	2.76 ± 0.44	0.60 ± 0.06	5.80 ± 0.93
060929	–	352.9 ± 5.4	527.3 ± 1.3	1261.8 ± 17.4	27.06 ± 0.56	31.11 ± 0.66	–	–
061121	1.314	71.5 ± 0.6	74.3 ± 0.4	79.4 ± 0.7	848.92 ± 62.72	45.61 ± 8.44	366.45 ± 27.08	19.70 ± 3.65
061202	–	90.2 ± 8.3	140.9 ± 1.2	363.6 ± 18.7	48.78 ± 1.83	21.84 ± 0.88	–	–

Table 1—Continued

GRB	z	T_{start} (s)	T_{peak} (s)	T_{end} (s)	F_p (10^{-10}erg cm^{-2} s^{-1})	S_F (10^{-8}erg cm^{-2})	L_p (10^{48}erg s^{-1})	$E_{x,iso}$ (10^{50}erg)
061202	–	211.0 ± 19.2	251.0 ± 4.6	591.7 ± 60.5	3.52 ± 0.40	3.90 ± 0.61	–	–
061202	–	246654.3 ± 4824.8	255026.7 ± 284.7	726419.8 ± 23583.9	0.00 ± 6.59E-4	2.45 ± 1.32	–	–
070103	2.6208	606.1 ± 103.4	797.9 ± 17.6	830.8 ± 18.2	0.23 ± 0.09	0.37 ± 0.32	0.35 ± 0.13	0.56 ± 0.48
070107	–	311.4 ± 2.3	321.8 ± 1.0	347.0 ± 1.0	15.71 ± 1.94	2.57 ± 0.40	–	–
070107	–	321.1 ± 8.7	357.7 ± 2.4	488.8 ± 19.7	16.84 ± 1.00	11.31 ± 1.16	–	–
070107	–	343.4 ± 25.6	447.2 ± 5.9	490.1 ± 11.1	6.15 ± 1.00	5.63 ± 1.71	–	–
070107	–	1311.6 ± 39.7	1348.2 ± 36.5	1442.8 ± 51.4	0.90 ± 0.22	0.97 ± 0.85	–	–
070107	–	83986.3 ± 4443.3	85339.9 ± 4524.4	96526.4 ± 5350.4	0.01 ± 0.00	1.09 ± 1.34	–	–
070129	2.3384	187.5 ± 69.1	210.2 ± 5.2	226.9 ± 12.9	8.71 ± 6.27	2.49 ± 5.28	10.74 ± 7.74	3.07 ± 6.51
070129	2.3384	217.1 ± 41.5	239.8 ± 7.2	631.8 ± 117.8	10.80 ± 7.38	7.37 ± 5.84	13.32 ± 9.11	9.08 ± 7.20
070129	2.3384	253.3 ± 9.4	304.7 ± 2.3	536.9 ± 57.2	76.30 ± 7.04	34.00 ± 3.29	94.09 ± 8.68	41.90 ± 4.06
070129	2.3384	261.2 ± 25.9	365.9 ± 1.7	467.6 ± 9.7	105.71 ± 7.53	45.97 ± 3.52	130.35 ± 9.28	56.70 ± 4.34
070129	2.3384	349.9 ± 15.2	445.6 ± 2.6	810.1 ± 61.9	39.33 ± 2.34	27.97 ± 1.73	48.50 ± 2.88	34.50 ± 2.13
070129	2.3384	368.8 ± 75.3	573.5 ± 8.9	1085.5 ± 101.4	14.27 ± 1.37	20.00 ± 2.02	17.60 ± 1.70	24.70 ± 2.49
070129	2.3384	623.2 ± 20.0	660.6 ± 3.7	924.9 ± 96.6	6.53 ± 0.88	3.73 ± 0.58	8.05 ± 1.09	4.60 ± 0.71
070129	2.3384	865.6 ± 4327.9	885.9 ± 0.9	1198.9 ± 196.5	0.36 ± 0.20	0.45 ± 0.36	0.45 ± 0.25	0.56 ± 0.45
070318	0.836	237.7 ± 6.1	280.7 ± 4.2	429.7 ± 9.2	7.78 ± 0.40	8.21 ± 0.80	1.38 ± 0.07	1.46 ± 0.14
070330	–	172.3 ± 9.1	215.9 ± 4.2	321.3 ± 16.3	3.37 ± 0.44	1.92 ± 0.32	–	–
070419B	–	188.5 ± 7.5	233.1 ± 2.5	440.0 ± 6.9	59.61 ± 2.68	64.22 ± 5.23	–	–
070518	–	71.7 ± 26.0	86.4 ± 1.8	92.2 ± 1.8	3.63 ± 1.47	0.54 ± 0.64	–	–
070518	–	91.9 ± 3.7	104.8 ± 1.2	251.3 ± 18.8	10.07 ± 1.14	3.67 ± 0.52	–	–
070518	–	135.9 ± 5.0	142.0 ± 2.7	166.7 ± 19.1	2.85 ± 0.89	0.41 ± 0.21	–	–
070518	–	148.6 ± 9.1	187.8 ± 1.9	281.8 ± 8.4	8.93 ± 0.58	3.44 ± 0.27	–	–
070520B	–	139.4 ± 4.0	195.5 ± 1.2	857.9 ± 4.2	27.08 ± 0.64	21.85 ± 0.62	–	–
070616	–	137.4 ± 9.0	148.8 ± 5.0	178.1 ± 15.8	42.62 ± 9.80	11.59 ± 6.83	–	–
070616	–	192.6 ± 5.2	198.5 ± 3.3	205.7 ± 5.9	23.24 ± 5.89	2.35 ± 1.92	–	–
070616	–	186.5 ± 54.5	265.7 ± 18.1	435.2 ± 99.7	36.65 ± 23.53	45.45 ± 40.53	–	–
070616	–	228.6 ± 123.3	400.3 ± 15.8	676.2 ± 65.8	57.56 ± 11.79	101.05 ± 28.60	–	–
070616	–	452.6 ± 8.1	488.9 ± 2.0	682.9 ± 40.3	68.16 ± 7.74	44.50 ± 6.27	–	–
070616	–	538.5 ± 3.9	548.6 ± 0.5	828.6 ± 61.6	29.69 ± 3.75	25.37 ± 4.69	–	–
070616	–	704.9 ± 14.4	754.8 ± 5.7	855.4 ± 29.5	11.34 ± 1.18	7.91 ± 1.42	–	–
070616	–	896.1 ± 1932.0	1101.2 ± 445.2	1325.8 ± 782.9	1.51 ± 1.54	5.49 ± 20.48	–	–
070704	–	250.9 ± 2.7	313.4 ± 1.0	1446.4 ± 11.5	61.67 ± 1.34	58.74 ± 1.38	–	–
070704	–	538.6 ± 139.8	671.9 ± 40.5	13501.8 ± 1040.2	1.53 ± 0.25	12.32 ± 2.41	–	–
070714A	–	10.3 ± 26.2	303.4 ± 54.7	719.3 ± 573.2	0.14 ± 0.05	0.51 ± 0.25	–	–
070714A	–	247.5 ± 460.3	869.8 ± 185.5	15491.5 ± 6455.1	0.07 ± 0.02	2.69 ± 1.48	–	–
070721B	3.626	232.9 ± 12.1	311.5 ± 0.9	330.2 ± 0.9	16.63 ± 1.49	6.62 ± 0.84	42.59 ± 3.81	17.00 ± 2.15
070721B	3.626	327.1 ± 4.7	346.7 ± 2.1	398.8 ± 13.8	8.66 ± 0.81	2.72 ± 0.43	22.18 ± 2.07	6.97 ± 1.09
070721B	3.626	422.0 ± 127.7	507.4 ± 97.7	592.8 ± 345.6	2.21 ± 0.87	2.58 ± 2.59	5.67 ± 2.23	6.60 ± 6.64
070721B	3.626	597.0 ± 55064.5	610.5 ± 54072.9	930.2 ± 70698.7	1.97 ± 461.80	3.58 ± 1655.92	5.05 ± 1182.58	9.17 ± 4240.00
070724A	0.457	22.1 ± 19.1	109.0 ± 2.2	136.7 ± 4.4	8.78 ± 0.88	5.54 ± 0.89	0.45 ± 0.05	0.29 ± 0.05
071021	2.452	164.0 ± 13.4	216.2 ± 2.1	319.7 ± 3.2	22.39 ± 1.07	13.74 ± 1.75	29.97 ± 1.43	18.40 ± 2.34
071021	2.452	5637.5 ± 137.5	6328.6 ± 62.0	8202.1 ± 174.3	0.35 ± 0.03	3.30 ± 0.39	0.46 ± 0.04	4.42 ± 0.52
071031	2.692	2.8 ± 3.5	158.0 ± 1.5	203.8 ± 9.8	47.26 ± 1.77	59.39 ± 3.11	74.16 ± 2.77	93.20 ± 4.89
071031	2.692	147.9 ± 16.4	200.9 ± 1.7	616.7 ± 106.3	29.31 ± 3.88	16.29 ± 2.30	45.99 ± 6.08	25.60 ± 3.61
071031	2.692	213.0 ± 13.6	258.3 ± 1.8	544.8 ± 53.5	13.61 ± 1.47	6.97 ± 0.82	21.36 ± 2.31	10.90 ± 1.29
071031	2.692	247.9 ± 18.1	448.8 ± 3.9	2985.7 ± 105.1	9.56 ± 0.28	24.30 ± 0.76	15.01 ± 0.44	38.10 ± 1.20
071112C	0.823	579.7 ± 37.6	657.9 ± 32.6	974.9 ± 46.2	1.58 ± 0.21	4.15 ± 1.30	0.27 ± 0.04	0.72 ± 0.22
071118	–	201.0 ± 8.8	209.6 ± 3.2	323.7 ± 70.3	2.20 ± 0.48	1.02 ± 0.39	–	–
071118	–	375.1 ± 20.2	401.0 ± 14.2	442.1 ± 31.5	2.01 ± 0.54	0.98 ± 0.72	–	–

Table 1—Continued

GRB	z	T_{start} (s)	T_{peak} (s)	T_{end} (s)	F_p (10^{-10}erg cm^{-2} s^{-1})	S_F (10^{-8}erg cm^{-2})	L_p (10^{48}erg s^{-1})	$E_{x,iso}$ (10^{50}erg)
071118	–	482.2 ± 36.3	599.7 ± 12.7	913.4 ± 41.0	4.06 ± 0.35	7.71 ± 1.08	–	–
071122	1.14	400.3 ± 968554.2	405.2 ± 727056.5	454.6 ± 789589.7	1.30 ± 24263.35	0.41 ± 12229.72	0.43 ± 7968.72	0.13 ± 4020.00
080210	2.641	166.6 ± 3.3	191.6 ± 1.3	255.1 ± 7.4	20.77 ± 1.58	6.00 ± 0.55	31.56 ± 2.40	9.11 ± 0.84
080212	–	177.7 ± 2.9	191.5 ± 2.1	325.9 ± 27.1	10.94 ± 1.00	4.10 ± 0.51	–	–
080212	–	195.2 ± 6.8	240.0 ± 1.4	591.9 ± 34.5	38.78 ± 2.76	24.86 ± 1.96	–	–
080212	–	218.0 ± 9.8	296.2 ± 1.5	573.7 ± 19.5	34.77 ± 2.08	23.94 ± 1.52	–	–
080229A	–	58.2 ± 7.1	107.7 ± 1.2	221.6 ± 13.1	62.56 ± 1.95	27.90 ± 1.13	–	–
080229A	–	299.5 ± 56.6	377.0 ± 38.1	706.7 ± 367.3	4.46 ± 0.90	13.06 ± 13.11	–	–
080310	2.4266	132.6 ± 3.5	147.3 ± 1.1	1772.9 ± 168.2	21.85 ± 2.51	21.98 ± 3.02	28.72 ± 3.29	28.90 ± 3.97
080310	2.4266	173.2 ± 6.4	191.3 ± 1.3	1423.4 ± 523.5	24.36 ± 3.44	21.70 ± 3.73	32.02 ± 4.52	28.50 ± 4.90
080310	2.4266	129.7 ± 46.3	233.3 ± 4.9	395.7 ± 28.3	20.00 ± 4.71	13.29 ± 3.63	26.29 ± 6.19	17.50 ± 4.77
080310	2.4266	265.4 ± 11.6	280.3 ± 1.8	394.7 ± 88.1	11.86 ± 2.95	2.21 ± 0.61	15.59 ± 3.88	2.90 ± 0.80
080310	2.4266	116.2 ± 42.3	365.6 ± 2.6	621.6 ± 7.7	36.35 ± 1.79	56.56 ± 4.04	47.79 ± 2.35	74.40 ± 5.31
080310	2.4266	340.7 ± 11.2	567.6 ± 1.6	991.2 ± 25.6	32.88 ± 0.90	31.69 ± 0.87	43.23 ± 1.18	41.70 ± 1.15
080310	2.4266	211.9 ± 938.4	6957.2 ± 1024.9	43685.4 ± 8325.0	0.09 ± 0.01	14.26 ± 2.58	0.11 ± 0.01	18.70 ± 3.39
080319A	–	1312.1 ± 43.6	1331.7 ± 33.0	1350.3 ± 34.6	0.12 ± 0.06	0.04 ± 0.13	–	–
080319D	–	93.4 ± 138.1	188.9 ± 23.8	258.4 ± 91.6	3.59 ± 1.50	2.72 ± 1.44	–	–
080319D	–	229.8 ± 37.2	325.1 ± 11.1	493.8 ± 41.5	6.90 ± 0.87	7.78 ± 1.45	–	–
080319D	–	397.6 ± 162.3	470.9 ± 18.5	696.5 ± 539.6	2.29 ± 0.82	1.42 ± 0.51	–	–
080319D	–	1252.9 ± 13664.3	2115.8 ± 10869.8	10785.5 ± 55847.2	0.10 ± 0.68	2.92 ± 33.26	–	–
080320	–	189.4 ± 5246.3	212.3 ± 97.3	249.7 ± 159.2	2.72 ± 4.52	0.80 ± 1.64	–	–
080320	–	273.5 ± 19.4	309.6 ± 4.2	487.0 ± 23.0	4.26 ± 0.42	3.10 ± 0.42	–	–
080320	–	753.4 ± 9240.5	763.0 ± 851.3	901.5 ± 975.6	0.78 ± 6.94	0.60 ± 8.57	–	–
080325	–	83.4 ± 35.0	167.2 ± 2.3	212.7 ± 14.5	33.55 ± 5.73	13.29 ± 2.56	–	–
080325	–	115.2 ± 17.1	218.5 ± 3.3	499.6 ± 80.1	38.58 ± 4.56	31.12 ± 3.87	–	–
080325	–	109.8 ± 93.5	319.3 ± 6.0	704.1 ± 24.3	12.60 ± 2.32	22.06 ± 4.41	–	–
080506	–	51.9 ± 27.7	174.6 ± 2.0	237.5 ± 3.4	28.75 ± 1.60	30.86 ± 4.00	–	–
080506	–	423.0 ± 9.0	476.3 ± 3.7	619.2 ± 11.7	9.17 ± 0.51	7.93 ± 0.70	–	–
080607	3.036	117.3 ± 0.8	124.7 ± 0.4	226.4 ± 1.7	212.57 ± 6.75	62.77 ± 2.61	407.79 ± 12.94	120.00 ± 5.00
080802	–	80.9 ± 3.1	93.7 ± 1.0	123.1 ± 3.4	15.27 ± 1.25	2.57 ± 0.30	–	–
080805	1.505	98.0 ± 2.3	118.0 ± 0.9	411.1 ± 2.8	32.95 ± 0.83	18.94 ± 0.67	18.37 ± 0.46	10.60 ± 0.37
080810	3.35	80.2 ± 2.0	105.3 ± 0.7	133.1 ± 1.7	66.51 ± 2.57	16.82 ± 1.02	149.91 ± 5.79	37.90 ± 2.29
080810	3.35	198.2 ± 1.7	208.5 ± 1.1	247.8 ± 3.5	17.50 ± 1.07	4.83 ± 0.57	39.44 ± 2.42	10.90 ± 1.28
080906	2	148.3 ± 6.5	175.6 ± 2.0	693.4 ± 6.9	14.85 ± 0.95	13.81 ± 1.20	13.92 ± 0.89	12.90 ± 1.13
080906	2	233.6 ± 66.0	614.1 ± 22.7	815.7 ± 324.0	1.55 ± 0.14	4.00 ± 1.00	1.45 ± 0.13	3.75 ± 0.94
080906	2	650.9 ± 144.4	1053.6 ± 49.7	8182.1 ± 598.0	0.95 ± 0.09	20.71 ± 2.84	0.89 ± 0.08	19.40 ± 2.66
080913	6.44	209.1 ± 553.9	415.0 ± 154.7	4949.0 ± 325.8	0.21 ± 0.11	0.84 ± 0.55	1.27 ± 0.65	5.19 ± 3.41
080913	6.44	645.0 ± 4.6E6	2859.5 ± 2E7	15510.0 ± 2E8	0.63 ± 19811.40	9.43 ± 298877.42	3.84 ± 121752.76	57.90 ± 1.84E6
080928	1.692	148.7 ± 3.5	208.6 ± 1.0	349.8 ± 3.8	162.54 ± 4.33	93.31 ± 2.87	112.57 ± 3.00	64.60 ± 1.99
080928	1.692	326.0 ± 2.9	356.4 ± 1.2	406.5 ± 4.2	23.10 ± 0.97	8.58 ± 0.58	16.00 ± 0.67	5.94 ± 0.40
081008	1.9685	279.9 ± 1.9	298.9 ± 0.9	420.1 ± 4.5	24.78 ± 1.01	10.74 ± 0.56	22.57 ± 0.92	9.78 ± 0.51
081028	–	285.1 ± 7.7	324.4 ± 2.7	3174.3 ± 20.2	53.40 ± 2.72	76.81 ± 5.49	–	–
081028	–	317.8 ± 252.2	544.8 ± 20.7	1337.4 ± 54.4	4.70 ± 1.97	11.52 ± 7.51	–	–
081028	–	582.7 ± 32.9	814.7 ± 4.0	6403.9 ± 1931.2	10.91 ± 0.61	46.02 ± 3.17	–	–
081028	–	4292.7 ± 1030.4	23172.6 ± 821.7	84690.3 ± 4139.3	0.09 ± 0.00	28.87 ± 1.82	–	–
081102	–	920.5 ± 9.8	965.3 ± 4.1	1791.4 ± 47.9	5.70 ± 0.40	9.81 ± 0.83	–	–
081210	–	120.0 ± 1.8	138.2 ± 0.7	183.8 ± 8.0	29.12 ± 1.47	5.90 ± 0.40	–	–
081210	–	155.7 ± 8.4	165.5 ± 1.8	176.7 ± 2.0	4.95 ± 1.25	0.57 ± 0.23	–	–
081210	–	98.8 ± 83.5	212.1 ± 4.1	265.0 ± 8.7	6.41 ± 1.50	6.87 ± 3.36	–	–
081210	–	252.7 ± 43.8	320.0 ± 9.8	383.1 ± 44.3	3.96 ± 1.27	2.99 ± 1.64	–	–

Table 1—Continued

GRB	z	T_{start} (s)	T_{peak} (s)	T_{end} (s)	F_p (10^{-10}erg cm^{-2} s^{-1})	S_F (10^{-8}erg cm^{-2})	L_p (10^{48}erg s^{-1})	$E_{x,iso}$ (10^{50}erg)
081210	–	362.5 ± 14.2	387.8 ± 4.8	451.0 ± 30.8	3.16 ± 0.89	1.70 ± 0.91	–	–
090111	–	287.5 ± 110.1	480.8 ± 23.8	1384.7 ± 195.3	2.99 ± 0.43	6.51 ± 1.03	–	–
090407	1.4485	115.0 ± 2.2	137.4 ± 1.0	191.9 ± 5.0	29.13 ± 1.13	9.10 ± 0.56	15.12 ± 0.59	4.72 ± 0.29
090407	1.4485	179.1 ± 11.0	244.8 ± 4.0	352.8 ± 17.0	10.96 ± 0.47	9.21 ± 0.89	5.69 ± 0.24	4.78 ± 0.46
090407	1.4485	285.1 ± 4.8	304.0 ± 1.7	338.5 ± 7.1	9.04 ± 0.81	2.32 ± 0.36	4.69 ± 0.42	1.20 ± 0.19
090417B	–	207.6 ± 33.8	510.6 ± 9.9	947.4 ± 37.5	19.72 ± 1.32	73.90 ± 7.51	–	–
090417B	–	1265.2 ± 10.0	1392.1 ± 4.7	2574.7 ± 112.9	16.52 ± 0.60	78.92 ± 5.26	–	–
090417B	–	1465.7 ± 12.5	1541.5 ± 6.7	1771.4 ± 149.3	16.76 ± 1.37	22.04 ± 3.91	–	–
090417B	–	1559.9 ± 46.2	1678.2 ± 5.9	1899.5 ± 42.0	14.87 ± 3.58	23.18 ± 7.21	–	–
090423	8	117.6 ± 6.8	165.6 ± 3.9	330.0 ± 29.0	4.51 ± 0.52	2.16 ± 0.27	37.81 ± 4.33	18.10 ± 2.27
090429A	–	88.5 ± 7.7	99.2 ± 3.1	225.7 ± 8.7	13.77 ± 3.29	3.20 ± 1.27	–	–
090429A	–	94.1 ± 35.4	131.9 ± 2.1	178.5 ± 5.2	8.25 ± 1.37	2.30 ± 0.67	–	–
090429A	–	105.3 ± 12.2	171.4 ± 1.9	514.6 ± 34.5	11.35 ± 0.68	6.01 ± 0.37	–	–
090429A	–	208.7 ± 18.3	256.1 ± 5.7	25353.3 ± 84447.3	3.09 ± 0.92	15.02 ± 6.56	–	–
090516	3.9	37.3 ± 28.5	196.5 ± 3.8	491.3 ± 12.9	83.99 ± 4.90	117.92 ± 8.17	241.50 ± 14.10	339.00 ± 23.50
090516	3.9	251.0 ± 1.9	273.2 ± 0.6	355.6 ± 5.1	128.22 ± 5.86	29.83 ± 1.50	368.67 ± 16.86	85.80 ± 4.32
090516	3.9	389.5 ± 0.7	391.9 ± 0.2	459.0 ± 13.9	3.02 ± 0.68	1.23 ± 0.51	8.69 ± 1.97	3.54 ± 1.46
090607	–	95.3 ± 9.3	118.5 ± 3.6	208.3 ± 39.9	3.53 ± 0.45	1.59 ± 0.36	–	–
090621A	–	208.9 ± 2.1	238.3 ± 0.6	501.8 ± 10.6	197.79 ± 12.55	80.71 ± 5.65	–	–
090621A	–	213.2 ± 8.3	267.8 ± 1.0	348.2 ± 12.0	224.71 ± 10.83	57.17 ± 2.83	–	–
090709A	–	74.9 ± 1.0	85.3 ± 0.5	112.2 ± 1.7	124.92 ± 5.75	21.73 ± 1.56	–	–
090709A	–	220.4 ± 15.0	277.6 ± 5.9	374.9 ± 45.4	8.21 ± 0.87	5.46 ± 0.99	–	–
090709A	–	322.7 ± 17.6	411.6 ± 5.1	2416.1 ± 173.0	10.95 ± 0.70	68.15 ± 7.29	–	–
090715B	3	58.0 ± 2.0	76.7 ± 0.7	103.6 ± 2.6	113.07 ± 5.14	21.64 ± 1.49	212.67 ± 9.66	40.70 ± 2.80
090715B	3	99.1 ± 2.7	109.2 ± 1.3	181.1 ± 18.1	26.38 ± 2.73	10.28 ± 2.23	49.62 ± 5.13	19.30 ± 4.19
090715B	3	153.5 ± 1.5	157.7 ± 0.9	169.2 ± 5.7	27.34 ± 4.75	2.19 ± 0.69	51.41 ± 8.94	4.13 ± 1.30
090715B	3	127.4 ± 15.0	179.3 ± 2.7	198.5 ± 7.2	32.96 ± 8.37	12.21 ± 4.59	62.00 ± 15.74	23.00 ± 8.63
090715B	3	180.6 ± 7.8	195.4 ± 1.2	263.0 ± 23.4	39.53 ± 7.41	12.24 ± 3.26	74.35 ± 13.94	23.00 ± 6.13
090715B	3	238.5 ± 2.6	252.2 ± 0.9	285.7 ± 9.5	79.61 ± 8.31	12.00 ± 1.54	149.74 ± 15.63	22.60 ± 2.90
090715B	3	201.5 ± 9.3	284.4 ± 1.0	368.5 ± 3.3	120.11 ± 5.41	60.65 ± 3.15	225.92 ± 10.18	114.00 ± 5.92
090715B	3	433.6 ± 5.8	435.9 ± 5.7	441.3 ± 6.4	1.81 ± 0.48	0.13 ± 0.31	3.40 ± 0.90	0.25 ± 0.58
090727	–	109.4 ± 10.9	268.5 ± 7.5	921.9 ± 305.8	37.48 ± 2.27	46.99 ± 3.01	–	–
090807	–	173.6 ± 1.2	186.7 ± 0.5	445.4 ± 1.3	49.73 ± 1.18	19.09 ± 0.61	–	–
090807	–	5450.4 ± 179.1	6121.8 ± 83.4	17576.9 ± 2398.1	0.06 ± 0.00	2.52 ± 0.39	–	–
090809	2.737	168.3 ± 2.0	181.0 ± 0.9	1145.1 ± 249.8	29.88 ± 2.60	22.78 ± 2.42	48.22 ± 4.20	36.80 ± 3.90
090809	2.737	2635.0 ± 229.6	4771.2 ± 94.7	10993.3 ± 1647.7	0.36 ± 0.02	8.12 ± 0.67	0.58 ± 0.04	13.10 ± 1.08
090809	2.737	6036.3 ± 5002.5	17179.2 ± 2230.1	80566.2 ± 19460.5	0.02 ± 0.00	5.21 ± 1.16	0.03 ± 0.00	8.41 ± 1.87
090812	2.452	105.8 ± 3.3	134.0 ± 1.4	257.5 ± 5.0	40.83 ± 2.00	27.53 ± 2.14	54.65 ± 2.67	36.80 ± 2.87
090812	2.452	241.8 ± 2.2	260.4 ± 1.1	344.9 ± 4.5	19.02 ± 0.69	9.64 ± 0.64	25.46 ± 0.92	12.90 ± 0.86
090831C	–	155.8 ± 6.6	181.9 ± 3.5	297.3 ± 17.9	2.71 ± 0.36	1.40 ± 0.25	–	–
090831C	–	384.6 ± 28.3	442.1 ± 16.7	560.7 ± 39.3	0.52 ± 0.12	0.51 ± 0.20	–	–
090904A	–	291.2 ± 1.4	304.1 ± 0.6	427.4 ± 1.8	52.12 ± 1.55	21.21 ± 0.89	–	–
090904B	–	153.3 ± 42.7	263.5 ± 15.2	1877.9 ± 136.3	2.63 ± 0.19	13.48 ± 1.50	–	–
090929B	–	92.1 ± 3.5	108.9 ± 2.1	156.5 ± 10.4	20.31 ± 1.43	7.12 ± 1.19	–	–
090929B	–	133.7 ± 2.0	151.5 ± 0.7	434.0 ± 21.3	44.64 ± 2.12	31.85 ± 2.09	–	–
091026	–	152.3 ± 8.4	174.7 ± 3.2	567.3 ± 12.4	5.52 ± 0.67	4.55 ± 0.72	–	–
091026	–	254.5 ± 13.6	334.7 ± 3.1	640.2 ± 70.3	8.98 ± 0.46	9.00 ± 0.71	–	–
091026	–	608.9 ± 39.3	775.3 ± 18.5	4148.1 ± 222.7	1.89 ± 0.12	20.24 ± 1.96	–	–
091029	2.752	277.8 ± 23.8	311.9 ± 11.4	429.7 ± 23.2	1.14 ± 0.28	0.85 ± 0.31	1.86 ± 0.45	1.38 ± 0.51
091104	–	191.4 ± 7.0	205.9 ± 2.4	407.3 ± 23.9	3.84 ± 0.65	3.01 ± 0.71	–	–

Table 1—Continued

GRB	z	T_{start} (s)	T_{peak} (s)	T_{end} (s)	F_p (10^{-10}erg cm^{-2} s^{-1})	S_F (10^{-8}erg cm^{-2})	L_p (10^{48}erg s^{-1})	$E_{x,iso}$ (10^{50}erg)
091130B	–	80.4 ± 3.3	98.7 ± 0.6	1333.0 ± 3.0	112.12 ± 2.29	65.94 ± 1.92	–	–
091221	–	93.5 ± 1.8	106.6 ± 0.8	190.8 ± 3.5	22.46 ± 1.03	6.59 ± 0.41	–	–
100117A	–	105.3 ± 26.6	193.1 ± 13.5	320.9 ± 35.0	17.76 ± 1.35	23.81 ± 5.32	–	–
100117A	–	296.0 ± 52.6	337.3 ± 11.4	1194.4 ± 161.6	6.34 ± 1.67	18.45 ± 6.99	–	–
100212A	–	64.8 ± 8.6	68.8 ± 1.9	88.2 ± 19.5	22.00 ± 38.69	2.53 ± 6.04	–	–
100212A	–	73.7 ± 3.8	80.5 ± 1.0	100.5 ± 10.2	50.65 ± 13.47	4.79 ± 1.59	–	–
100212A	–	84.9 ± 7.4	101.7 ± 2.3	363.0 ± 149.0	59.09 ± 16.01	21.88 ± 6.64	–	–
100212A	–	94.2 ± 9.6	121.7 ± 1.8	313.9 ± 56.0	85.76 ± 21.79	29.76 ± 8.02	–	–
100212A	–	168.0 ± 4.5	174.3 ± 1.6	244.6 ± 63.5	9.78 ± 2.92	2.09 ± 0.81	–	–
100212A	–	184.7 ± 9.0	197.3 ± 1.9	272.1 ± 34.4	10.23 ± 3.24	2.47 ± 0.93	–	–
100212A	–	217.7 ± 1.9	225.8 ± 0.5	310.1 ± 16.2	26.23 ± 2.46	4.91 ± 0.55	–	–
100212A	–	243.4 ± 1.9	250.5 ± 0.5	349.2 ± 21.5	22.84 ± 2.34	4.78 ± 0.59	–	–
100212A	–	271.4 ± 4.8	279.9 ± 1.2	465.8 ± 49.7	8.23 ± 1.37	3.49 ± 0.74	–	–
100212A	–	335.9 ± 3.2	350.9 ± 0.9	440.6 ± 12.2	12.15 ± 1.05	2.92 ± 0.29	–	–
100212A	–	400.9 ± 7.3	422.2 ± 2.3	515.7 ± 27.8	3.92 ± 0.58	1.34 ± 0.25	–	–
100212A	–	577.9 ± 29.9	665.5 ± 7.5	811.2 ± 33.9	2.79 ± 0.49	2.08 ± 0.41	–	–
100302A	4.813	18.0 ± 17.4	133.7 ± 3.0	273.0 ± 39.5	18.60 ± 1.67	9.80 ± 0.93	74.11 ± 6.65	39.00 ± 3.69
100302A	4.813	118.2 ± 20.9	186.2 ± 2.6	391.8 ± 51.5	6.93 ± 0.67	3.09 ± 0.31	27.63 ± 2.66	12.30 ± 1.23
100302A	4.813	212.8 ± 4.1	251.5 ± 0.7	463.0 ± 17.3	24.46 ± 0.97	7.70 ± 0.33	97.47 ± 3.86	30.70 ± 1.30
100302A	4.813	277.5 ± 6.1	313.8 ± 0.9	1105.3 ± 51.9	10.19 ± 0.38	8.52 ± 0.38	40.60 ± 1.53	33.90 ± 1.50
100302A	4.813	487.7 ± 11.4	503.4 ± 1.7	770.2 ± 91.1	1.24 ± 0.36	0.71 ± 0.25	4.94 ± 1.43	2.85 ± 1.00
100513A	4.772	166.6 ± 22.9	227.2 ± 8.6	980.8 ± 19.2	2.04 ± 0.14	3.17 ± 0.38	8.01 ± 0.56	12.40 ± 1.48
100526A	–	171.3 ± 2.6	186.7 ± 1.0	538.6 ± 2.9	28.40 ± 2.00	17.41 ± 1.59	–	–
100606A	–	96.2 ± 7.6	124.9 ± 2.1	462.9 ± 62.5	11.87 ± 0.71	14.43 ± 1.86	–	–
100614A	–	158.1 ± 1.1	162.2 ± 0.4	217.4 ± 14.2	17.05 ± 1.51	3.91 ± 0.66	–	–
100614A	–	189.7 ± 5.7	203.1 ± 1.7	246.8 ± 12.5	8.61 ± 1.16	2.06 ± 0.43	–	–
100614A	–	258.4 ± 14.3	302.4 ± 4.8	499.7 ± 63.0	3.45 ± 0.32	3.30 ± 0.58	–	–
100614A	–	986.9 ± 37.5	1021.8 ± 28.9	1095.4 ± 39.7	0.40 ± 0.12	0.37 ± 0.37	–	–
100619A	–	29.5 ± 4.9	88.3 ± 0.7	151.1 ± 1.7	438.19 ± 22.05	143.14 ± 7.86	–	–
100619A	–	850.4 ± 3.7	949.0 ± 1.2	1564.4 ± 12.0	30.89 ± 0.54	44.94 ± 0.89	–	–
100704A	3.6	45.8 ± 7.8	113.4 ± 2.1	175.4 ± 12.9	34.19 ± 1.71	19.79 ± 1.61	86.56 ± 4.33	50.10 ± 4.08
100704A	3.6	112.5 ± 2.6	175.9 ± 0.6	371.2 ± 3.0	418.95 ± 9.64	187.53 ± 4.43	1060.55 ± 24.39	475.00 ± 11.20
100725B	–	80.9 ± 3.8	90.2 ± 1.3	153.7 ± 6.1	89.20 ± 7.97	13.98 ± 1.79	–	–
100725B	–	89.9 ± 6.6	128.6 ± 1.7	457.9 ± 14.1	115.75 ± 7.76	57.51 ± 4.15	–	–
100725B	–	114.3 ± 7.7	159.8 ± 1.3	357.4 ± 34.9	146.67 ± 7.76	52.74 ± 2.94	–	–
100725B	–	163.1 ± 4.1	215.7 ± 0.6	326.1 ± 6.6	256.22 ± 8.98	66.22 ± 2.36	–	–
100725B	–	252.4 ± 3.1	271.6 ± 0.6	361.2 ± 4.6	84.85 ± 4.62	16.19 ± 0.95	–	–
100727A	–	171.3 ± 7.3	245.5 ± 1.8	511.9 ± 7.0	12.35 ± 0.46	9.13 ± 0.39	–	–
100728A	1.567	64.3 ± 24.6	90.1 ± 5.6	119.1 ± 14.2	162.58 ± 23.17	54.19 ± 22.05	97.74 ± 13.93	32.60 ± 13.30
100728A	1.567	108.9 ± 4.8	122.1 ± 1.1	159.1 ± 4.6	170.61 ± 23.94	42.14 ± 8.89	102.57 ± 14.39	25.30 ± 5.34
100728A	1.567	181.8 ± 8.5	224.6 ± 2.9	257.1 ± 10.0	64.95 ± 4.13	31.33 ± 5.95	39.05 ± 2.48	18.80 ± 3.57
100728A	1.567	253.7 ± 7.6	267.3 ± 2.9	287.6 ± 7.5	42.08 ± 7.73	9.74 ± 4.31	25.30 ± 4.65	5.85 ± 2.59
100728A	1.567	293.9 ± 3.3	317.5 ± 1.0	376.8 ± 4.2	111.86 ± 5.09	40.78 ± 2.93	67.25 ± 3.06	24.50 ± 1.76
100728A	1.567	383.0 ± 0.7	389.4 ± 0.3	422.6 ± 2.2	95.79 ± 5.11	16.10 ± 1.26	57.58 ± 3.07	9.68 ± 0.76
100728A	1.567	451.2 ± 3.1	462.4 ± 2.1	480.4 ± 4.5	24.57 ± 2.56	4.94 ± 1.33	14.77 ± 1.54	2.97 ± 0.80
100728A	1.567	511.5 ± 3.2	570.1 ± 1.2	659.3 ± 4.9	102.62 ± 2.82	61.04 ± 2.37	61.69 ± 1.70	36.70 ± 1.42
100728A	1.567	673.9 ± 5.5	707.6 ± 3.0	809.1 ± 8.9	23.71 ± 1.14	18.96 ± 2.05	14.25 ± 0.69	11.40 ± 1.23
100802A	–	228.9 ± 7.6	507.3 ± 3.5	2007.1 ± 9.7	41.60 ± 1.01	101.36 ± 2.77	–	–
100805A	–	500.9 ± 14.4	621.0 ± 8.0	7132.7 ± 940.7	2.91 ± 0.18	16.84 ± 1.36	–	–
100807A	–	65.5 ± 4.6	91.4 ± 1.5	175.5 ± 8.1	8.15 ± 0.61	2.30 ± 0.19	–	–

Table 1—Continued

GRB	z	T_{start} (s)	T_{peak} (s)	T_{end} (s)	F_p (10^{-10}erg cm^{-2} s^{-1})	S_F (10^{-8}erg cm^{-2})	L_p (10^{48}erg s^{-1})	$E_{x,iso}$ (10^{50}erg)
100816A	0.8034	113.5 ± 13.6	143.3 ± 5.4	2277.1 ± 13.0	3.88 ± 0.44	3.38 ± 0.56	0.64 ± 0.07	0.56 ± 0.09
100816A	0.8034	269.3 ± 5.3E6	276.2 ± 504069.8	40217.8 ± 6E6	0.53 ± 892.15	5.07 ± 13430.54	0.09 ± 146.51	0.83 ± 2210.00
100816A	0.8034	3082.8 ± 4883.4	5960.2 ± 985.8	66077.6 ± 22951.7	0.01 ± 0.01	1.76 ± 2.93	0.00 ± 0.00	0.29 ± 0.48
100901A	1.408	163.2 ± 73.3	210.6 ± 31.1	399.3 ± 241.0	9.28 ± 1.29	7.30 ± 1.72	4.57 ± 0.63	3.59 ± 0.85
100901A	1.408	245.5 ± 36.5	251.2 ± 9.6	328.3 ± 91.9	4.99 ± 1.19	1.66 ± 0.76	2.45 ± 0.58	0.81 ± 0.37
100901A	1.408	285.5 ± 11.2	312.1 ± 3.6	567.9 ± 214.4	5.70 ± 1.24	5.31 ± 1.88	2.80 ± 0.61	2.61 ± 0.92
100901A	1.408	322.9 ± 9.6	396.3 ± 1.5	866.3 ± 47.8	21.07 ± 1.23	24.56 ± 1.69	10.37 ± 0.60	12.10 ± 0.83
100901A	1.408	957.2 ± 525.8	27381.3 ± 1224.0	154731.6 ± 10176.8	0.12 ± 0.00	69.53 ± 3.98	0.06 ± 0.00	34.20 ± 1.96
100901A	1.408	637634.5 ± 90242.0	693788.2 ± 76709.5	838632.2 ± 144255.3	0.00 ± 0.01	5.17 ± 11.96	0.00 ± 0.00	2.54 ± 5.89
100902A	4.5	356.0 ± 1.4	405.5 ± 0.9	564.5 ± 3.0	515.04 ± 12.41	274.06 ± 8.48	1851.49 ± 44.61	985.00 ± 30.50
100905A	–	249.3 ± 9.1	318.6 ± 3.2	463.0 ± 33.8	5.44 ± 0.47	3.14 ± 0.30	–	–
100905A	–	356.8 ± 18.6	405.2 ± 4.2	535.1 ± 20.9	5.25 ± 0.90	2.41 ± 0.45	–	–
100906A	1.727	76.6 ± 2.1	119.6 ± 0.6	207.2 ± 1.2	961.07 ± 34.70	312.31 ± 12.66	691.02 ± 24.95	225.00 ± 9.10
110102A	–	195.0 ± 0.8	205.8 ± 0.4	412.5 ± 3.2	262.10 ± 8.00	97.02 ± 3.52	–	–
110102A	–	213.7 ± 3.9	269.5 ± 0.8	375.5 ± 2.5	259.30 ± 7.94	104.00 ± 3.52	–	–
110119A	–	64.1 ± 40.3	78.4 ± 3.9	331.9 ± 4.5	36.04 ± 6.77	12.01 ± 16.45	–	–
110119A	–	71.8 ± 9.6	128.2 ± 1.4	360.8 ± 12.6	48.55 ± 1.76	18.66 ± 0.78	–	–
110119A	–	151.6 ± 16.5	168.7 ± 0.3	293.7 ± 230.0	15.84 ± 2.74	1.64 ± 0.32	–	–
110119A	–	82.9 ± 13.2	202.0 ± 2.2	437.4 ± 103.4	54.28 ± 3.76	28.63 ± 2.00	–	–
110119A	–	150.8 ± 25.8	235.9 ± 0.8	315.1 ± 1.4	28.59 ± 4.24	3.84 ± 0.57	–	–
110119A	–	91.0 ± 60.5	259.4 ± 2.5	378.1 ± 41.9	18.62 ± 3.35	8.42 ± 1.57	–	–
110119A	–	125.1 ± 124.3	335.2 ± 11.7	465.6 ± 2494.6	1.93 ± 0.68	1.27 ± 0.51	–	–
110119A	–	343.3 ± 24.4	385.9 ± 2.3	502.1 ± 161.1	3.16 ± 0.54	1.56 ± 0.46	–	–
110119A	–	505.3 ± 26.0	633.8 ± 13.0	2615.3 ± 90.3	2.83 ± 0.17	19.17 ± 1.66	–	–
110205A	1.98	132.7 ± 17.5	238.5 ± 2.7	379.4 ± 3.4	107.58 ± 3.93	167.60 ± 22.00	99.01 ± 3.62	154.00 ± 20.20
110205A	1.98	459.1 ± 7.1	472.3 ± 2.7	546.6 ± 24.0	5.02 ± 0.88	1.80 ± 0.48	4.62 ± 0.81	1.66 ± 0.45
110205A	1.98	600.7 ± 1.8	610.2 ± 1.4	648.5 ± 3.3	13.51 ± 0.82	4.29 ± 0.59	12.44 ± 0.75	3.95 ± 0.55
110407A	–	408.8 ± 4.1	441.6 ± 2.3	3919.7 ± 16.5	7.77 ± 0.28	17.51 ± 0.80	–	–
110407A	–	4498.2 ± 1656.1	4953.0 ± 585.8	5313.9 ± 745.7	0.02 ± 0.01	0.11 ± 0.18	–	–
110414A	–	28.9 ± 38.8	145.3 ± 2.7	200.8 ± 5.4	28.82 ± 2.49	25.05 ± 2.94	–	–
110414A	–	70.5 ± 42.7	365.4 ± 19.9	801.8 ± 484.4	1.77 ± 0.19	4.30 ± 0.76	–	–
110414A	–	167.4 ± 334.8	1853.9 ± 218.1	9165.3 ± 1269.8	0.23 ± 0.04	7.91 ± 1.59	–	–
110520A	–	155.0 ± 21.7	243.2 ± 11.6	408.6 ± 22.4	4.15 ± 0.56	5.03 ± 1.04	–	–
110709A	–	88.7 ± 4532.7	89.3 ± 4479.9	98.2 ± 4615.6	13.07 ± 3873.71	0.94 ± 760.15	–	–
110709A	–	180.6 ± 24.1	218.8 ± 8.2	795.6 ± 271.6	1.81 ± 0.33	3.64 ± 1.28	–	–
110709B	–	142.3 ± 32.5	153.3 ± 6.2	1659.9 ± 650.3	3.83 ± 0.96	14.83 ± 7.62	–	–
110709B	–	477.2 ± 4.8	658.9 ± 2.4	843.8 ± 16.8	98.48 ± 2.90	110.58 ± 3.72	–	–
110709B	–	651.7 ± 20.8	847.2 ± 2.5	936.2 ± 11.1	62.31 ± 2.47	58.91 ± 3.09	–	–
110709B	–	887.4 ± 10.6	935.7 ± 2.4	1230.2 ± 14.9	21.11 ± 1.01	25.83 ± 1.75	–	–
110709B	–	1271.0 ± 5.6	1305.0 ± 2.9	1474.4 ± 13.7	8.29 ± 0.57	7.88 ± 0.86	–	–
110801A	1.858	192.3 ± 5.2	214.0 ± 3.1	244.2 ± 5.2	10.85 ± 0.89	3.95 ± 0.87	8.91 ± 0.73	3.24 ± 0.71
110801A	1.858	317.2 ± 1.4	358.5 ± 0.6	624.8 ± 4.9	195.88 ± 4.83	117.05 ± 3.20	160.83 ± 3.97	96.10 ± 2.62
110820A	–	149.2 ± 2.7	257.9 ± 0.7	384.8 ± 3.5	97.19 ± 2.29	46.60 ± 1.14	–	–
110921A	–	197.6 ± 16.1	234.0 ± 10.0	289.1 ± 16.9	2.05 ± 0.38	1.17 ± 0.43	–	–
110921A	–	474.6 ± 16.9	516.1 ± 7.5	640.9 ± 25.6	1.89 ± 0.31	1.45 ± 0.36	–	–
111016A	–	391.6 ± 2.4	416.2 ± 1.0	560.2 ± 25.1	24.28 ± 1.31	9.93 ± 0.65	–	–
111016A	–	406.0 ± 13.2	483.1 ± 2.3	765.0 ± 41.3	27.45 ± 1.82	22.46 ± 1.68	–	–
111016A	–	414.4 ± 23.1	611.7 ± 2.2	925.6 ± 9.9	33.90 ± 1.03	42.54 ± 1.48	–	–
111016A	–	711.8 ± 7.3	792.8 ± 1.7	4713.5 ± 128.0	13.27 ± 0.28	49.78 ± 1.29	–	–
111103B	–	99.7 ± 0.8	116.8 ± 0.4	632.5 ± 4.5	155.12 ± 4.38	54.60 ± 1.71	–	–

Table 1—Continued

GRB	z	T_{start} (s)	T_{peak} (s)	T_{end} (s)	F_p (10^{-10}erg cm^{-2} s^{-1})	S_F (10^{-8}erg cm^{-2})	L_p (10^{48}erg s^{-1})	$E_{x,iso}$ (10^{50}erg)
111103B	–	179.8 ± 8.2	220.0 ± 2.6	2658.3 ± 266.3	12.36 ± 0.72	33.71 ± 2.74	–	–
111103B	–	330.6 ± 7.6	346.8 ± 2.0	547.9 ± 61.9	6.07 ± 1.04	2.29 ± 0.45	–	–
111103B	–	1600.3 ± 1492.4	5759.4 ± 359.0	41159.1 ± 3296.7	0.57 ± 0.04	72.58 ± 8.16	–	–
111107A	2.893	194.3 ± 50.9	324.3 ± 21.7	573.1 ± 47.8	0.88 ± 0.17	1.47 ± 0.41	1.55 ± 0.29	2.61 ± 0.73
111209A	0.677	1154.4 ± 45.9	1345.0 ± 28.8	2130.8 ± 89.3	38.17 ± 3.90	250.11 ± 54.16	4.43 ± 0.45	29.00 ± 6.29
111209A	0.677	1756.8 ± 16.4	2039.8 ± 4.5	2164.4 ± 4.7	112.79 ± 2.90	212.27 ± 8.99	13.09 ± 0.34	24.60 ± 1.04
111209A	0.677	5364.5 ± 7.9	5477.9 ± 2.1	7628.7 ± 90.9	20.70 ± 0.92	298.02 ± 25.19	2.40 ± 0.11	34.60 ± 2.92
111209A	0.677	11978.8 ± 84.3	12064.2 ± 80.5	12231.4 ± 87.9	6.87 ± 0.29	17.13 ± 16.73	0.80 ± 0.03	1.99 ± 1.94
111215A	–	644.2 ± 8.1	663.0 ± 6.1	679.7 ± 6.6	7.43 ± 0.53	2.50 ± 1.44	–	–
111215A	–	937.7 ± 3.1	972.5 ± 2.1	1107.0 ± 8.6	18.78 ± 0.56	20.75 ± 1.63	–	–
120102A	–	234.4 ± 383844.3	252.6 ± 99010.2	3563.9 ± 1.4E6	2.16 ± 604.98	17.54 ± 13071.86	–	–
120102A	–	963.5 ± 22.1	1067.5 ± 10.6	22205.5 ± 123.1	7.73 ± 0.25	108.72 ± 4.25	–	–
120211A	–	1708.1 ± 2614.3	6720.0 ± 1279.3	53064.6 ± 19609.9	0.03 ± 0.00	4.77 ± 1.26	–	–
120215A	–	1903.4 ± 1213.1	12593.9 ± 1779.6	142910.6 ± 36778.5	0.02 ± 0.00	7.11 ± 1.43	–	–
120308A	–	111.8 ± 1.8	124.5 ± 0.7	406.1 ± 3.1	49.05 ± 2.10	26.09 ± 1.39	–	–
120514A	–	73.9 ± 14.9	98.6 ± 3.4	122.1 ± 9.1	64.40 ± 9.76	13.75 ± 3.16	–	–
120514A	–	122.6 ± 6.7	142.3 ± 0.7	347.0 ± 54.5	88.75 ± 3.33	27.76 ± 1.08	–	–
120514A	–	346.8 ± 106.0	664.5 ± 69.6	5049.8 ± 760.4	0.50 ± 0.06	6.96 ± 1.42	–	–
120612A	–	216.5 ± 836.0	3581.6 ± 1730.5	13791.0 ± 6781.3	0.08 ± 0.07	4.69 ± 4.86	–	–
120701A	–	276.7 ± 466574.0	280.5 ± 465663.1	332.2 ± 497200.8	0.65 ± 2103.36	0.30 ± 5329.01	–	–
120728A	–	398.7 ± 45.7	549.0 ± 15.0	997.6 ± 69.6	1.37 ± 0.22	2.17 ± 0.38	–	–
120802A	3.796	140.3 ± 174.1	1315.2 ± 308.8	37706.7 ± 19040.3	0.11 ± 0.02	9.99 ± 4.32	0.30 ± 0.05	27.50 ± 11.90
121024A	2.298	181.9 ± 7.2	209.6 ± 3.4	251.4 ± 8.8	6.41 ± 0.49	2.52 ± 0.45	7.67 ± 0.59	3.02 ± 0.54
121024A	2.298	254.6 ± 6.9	273.1 ± 3.0	324.0 ± 10.7	4.02 ± 0.46	1.54 ± 0.35	4.81 ± 0.56	1.85 ± 0.42
121027A	1.773	195.9 ± 6.5	270.4 ± 3.0	945.7 ± 6.6	16.09 ± 0.57	21.92 ± 1.05	12.14 ± 0.43	16.50 ± 0.80
121027A	1.773	1118.8 ± 19.6	1260.2 ± 21.3	56984.3 ± 13950.7	77.62 ± 65.21	747.71 ± 757.26	58.55 ± 49.19	564.00 ± 571.00
121027A	1.773	2402.1 ± 447.2	6954.9 ± 102.3	35918.7 ± 4070.7	35.37 ± 4.44	959.04 ± 121.58	26.68 ± 3.35	723.00 ± 91.70
121027A	1.773	18575.2 ± 35526.4	98927.8 ± 22537.2	590967.4 ± 144614.2	0.02 ± 0.00	35.14 ± 12.88	0.01 ± 0.00	26.50 ± 9.72
121028A	–	690.6 ± 30.7	775.0 ± 16.8	1174.8 ± 66.3	0.81 ± 0.15	1.39 ± 0.32	–	–
121108A	–	121.3 ± 1.6	138.9 ± 0.4	198.4 ± 2.9	63.66 ± 2.68	11.66 ± 0.54	–	–
121123A	–	143.8 ± 3.0	246.6 ± 0.9	1790.9 ± 84.8	112.13 ± 1.86	134.21 ± 2.43	–	–
121125A	–	90.8 ± 0.6	92.7 ± 0.5	107.9 ± 1.4	15.49 ± 1.07	1.83 ± 0.33	–	–
121128A	2.2	75.1 ± 5.7	95.9 ± 1.7	120.7 ± 3.5	18.35 ± 1.34	4.77 ± 0.76	20.35 ± 1.48	5.29 ± 0.85
121211A	1.023	116.7 ± 3.3	166.8 ± 1.3	864.7 ± 7.0	119.36 ± 2.86	110.50 ± 3.09	31.72 ± 0.76	29.40 ± 0.82
121212A	–	173.3 ± 16.9	237.5 ± 5.6	419.2 ± 24.2	4.79 ± 0.52	3.60 ± 0.46	–	–
121212A	–	513.2 ± 15.3	559.1 ± 6.0	824.6 ± 35.5	1.96 ± 0.26	1.96 ± 0.33	–	–
121217A	–	300.3 ± 10.3	751.4 ± 3.1	1448.4 ± 21.2	46.43 ± 1.03	120.38 ± 2.77	–	–
121229A	2.707	348.4 ± 5.1	445.5 ± 3.5	979.5 ± 15.7	17.98 ± 0.66	22.88 ± 1.03	28.49 ± 1.04	36.20 ± 1.63
130131A	–	152.7 ± 7.4	193.5 ± 1.9	229.5 ± 8.0	9.04 ± 0.92	2.20 ± 0.26	–	–
130131A	–	173.1 ± 4.4	282.2 ± 1.1	468.1 ± 6.5	29.33 ± 0.81	18.54 ± 0.53	–	–
130211A	–	17.6 ± 4.1	216.1 ± 2.4	567.7 ± 18.1	9.30 ± 0.37	10.57 ± 0.45	–	–
130427B	2.78	115.3 ± 3.4	128.9 ± 1.5	169.8 ± 3.0	9.62 ± 0.64	2.63 ± 0.33	15.93 ± 1.06	4.36 ± 0.55
130514A	3.6	147.5 ± 18.7	236.9 ± 2.7	464.1 ± 4.0	86.70 ± 2.49	104.53 ± 12.91	219.48 ± 6.31	265.00 ± 32.70
130514A	3.6	276.4 ± 12.7	373.5 ± 2.0	494.5 ± 7.2	33.96 ± 1.40	23.77 ± 1.23	85.96 ± 3.56	60.20 ± 3.11
130528A	–	545.2 ± 15.3	697.2 ± 9.6	1316.8 ± 76.2	9.57 ± 0.51	23.62 ± 1.70	–	–
130528A	–	978.9 ± 6.8	1032.1 ± 2.0	1965.7 ± 79.9	16.58 ± 0.67	33.13 ± 1.75	–	–
130528A	–	1243.6 ± 10.6	1309.2 ± 2.5	2169.9 ± 163.9	9.52 ± 0.64	21.18 ± 1.96	–	–
130606A	5.91	83.6 ± 55.8	90.7 ± 60.1	96.8 ± 63.7	26.74 ± 345.15	1.88 ± 29.12	144.91 ± 1870.72	10.20 ± 158.00
130606A	5.91	73.0 ± 26.5	161.3 ± 1.6	181.9 ± 4.0	23.84 ± 2.42	15.13 ± 3.28	129.21 ± 13.11	82.00 ± 17.80
130606A	5.91	196.7 ± 5.7	222.1 ± 1.8	253.1 ± 8.8	28.54 ± 2.57	6.96 ± 0.98	154.70 ± 13.92	37.70 ± 5.31

Table 1—Continued

GRB	z	T_{start} (s)	T_{peak} (s)	T_{end} (s)	F_p (10^{-10}erg cm^{-2} s^{-1})	S_F (10^{-8}erg cm^{-2})	L_p (10^{48}erg s^{-1})	$E_{x,iso}$ (10^{50}erg)
130606A	5.91	240.7 ± 3.5	258.8 ± 1.0	383.8 ± 15.4	38.54 ± 2.26	17.79 ± 1.53	208.90 ± 12.26	96.40 ± 8.31
130606A	5.91	347.0 ± 12.4	411.1 ± 3.0	472.1 ± 9.5	16.69 ± 1.08	9.50 ± 1.03	90.48 ± 5.87	51.50 ± 5.59
130609B	–	127.4 ± 1.6	179.0 ± 0.9	304.2 ± 10.6	401.12 ± 13.62	184.76 ± 7.04	–	–
130609B	–	199.7 ± 9.8	276.9 ± 1.6	436.9 ± 5.6	136.37 ± 4.33	105.00 ± 4.25	–	–
130615A	–	36.7 ± 8.2	262.0 ± 6.9	936.9 ± 23.3	39.69 ± 1.98	96.41 ± 6.69	–	–
130722A	–	215.9 ± 6.3	268.6 ± 2.3	303.9 ± 5.0	24.20 ± 1.08	14.51 ± 1.86	–	–
130722A	–	318.2 ± 7.6	344.4 ± 2.7	378.5 ± 4.6	15.37 ± 0.92	6.34 ± 1.22	–	–
130803A	–	453.2 ± 32.3	502.6 ± 17.2	859.7 ± 128.7	1.83 ± 0.32	2.78 ± 0.76	–	–
130925A	0.347	638.2 ± 7.6	980.6 ± 2.0	1184.1 ± 4.9	47.12 ± 0.57	126.79 ± 2.64	1.38 ± 0.02	3.70 ± 0.08
130925A	0.347	1298.2 ± 3.2	1374.4 ± 1.1	1748.8 ± 14.2	61.72 ± 1.23	80.76 ± 2.06	1.80 ± 0.04	2.36 ± 0.06
130925A	0.347	4657.6 ± 6.6	5003.2 ± 2.0	5580.0 ± 11.6	47.67 ± 0.59	121.05 ± 1.67	1.39 ± 0.02	3.54 ± 0.05
130925A	0.347	6517.7 ± 11.0	7117.8 ± 5.8	8214.8 ± 97.7	50.94 ± 1.05	225.19 ± 5.29	1.49 ± 0.03	6.58 ± 0.15
130925A	0.347	10094.5 ± 92.1	11236.3 ± 7.7	11903.5 ± 8.1	7.58 ± 0.19	54.57 ± 2.03	0.22 ± 0.01	1.59 ± 0.06
131004A	0.717	752.1 ± 18.1	775.5 ± 15.8	876.7 ± 35.7	0.93 ± 0.24	0.81 ± 0.49	0.12 ± 0.03	0.11 ± 0.06
131030A	1.293	22.4 ± 4.5	112.2 ± 1.0	268.8 ± 2.4	704.26 ± 21.42	535.48 ± 18.89	294.80 ± 8.96	224.00 ± 7.91
131103A	0.599	372.2 ± 38179.4	379.7 ± 0.4	571.6 ± 60.3	2.70 ± 0.80	1.98 ± 0.88	0.24 ± 0.07	0.18 ± 0.08
131103A	0.599	644.1 ± 2.1	683.3 ± 0.7	2092.4 ± 44.1	50.70 ± 1.66	81.18 ± 3.18	4.58 ± 0.15	7.33 ± 0.29
131117A	4.042	82.7 ± 2.1	94.8 ± 0.8	133.6 ± 3.8	13.01 ± 1.05	2.03 ± 0.20	39.59 ± 3.19	6.19 ± 0.59
131127A	–	439.3 ± 31.2	799.0 ± 24.0	5412.2 ± 297.3	0.55 ± 0.02	8.33 ± 0.59	–	–
140108A	–	64.3 ± 1.5	86.7 ± 0.4	135.7 ± 1.7	284.71 ± 11.63	49.42 ± 2.14	–	–
140108A	–	206.1 ± 2.4	219.1 ± 1.4	309.1 ± 7.6	10.96 ± 0.62	5.62 ± 0.60	–	–
140114A	3	18.0 ± 6.1	194.6 ± 2.3	308.1 ± 6.4	117.92 ± 3.61	181.61 ± 7.61	221.80 ± 6.79	342.00 ± 14.30
140114A	3	261.1 ± 5.5	321.7 ± 0.7	985.3 ± 26.3	49.66 ± 1.23	31.95 ± 0.87	93.40 ± 2.32	60.10 ± 1.64
140206A	2.73	45.6 ± 0.9	59.7 ± 0.4	115.5 ± 1.6	550.56 ± 19.70	97.38 ± 3.91	884.58 ± 31.65	156.00 ± 6.28
140206A	2.73	176.3 ± 1.4	222.4 ± 0.7	345.7 ± 2.7	132.74 ± 2.81	74.26 ± 1.87	213.27 ± 4.52	119.00 ± 3.00
140301A	1.416	517.4 ± 11.9	577.3 ± 3.5	951.9 ± 39.5	2.46 ± 0.17	2.79 ± 0.24	1.23 ± 0.09	1.39 ± 0.12
140304A	5.283	141.6 ± 55.0	341.1 ± 38.5	10968.1 ± 288.0	3.34 ± 0.47	14.73 ± 2.27	15.34 ± 2.15	67.60 ± 10.40
140304A	5.283	585.1 ± 182.0	790.8 ± 28.4	11894.2 ± 9699.8	1.52 ± 0.27	10.35 ± 2.37	6.97 ± 1.25	47.50 ± 10.90
140304A	5.283	12195.1 ± 9283.6	16412.1 ± 8835.7	77929.8 ± 43627.1	0.05 ± 0.04	10.21 ± 11.49	0.23 ± 0.17	46.80 ± 52.70
140413A	–	1838.2 ± 35.7	2512.2 ± 9.2	17144.7 ± 180.5	14.03 ± 0.22	217.99 ± 3.92	–	–
140430A	1.6	148.4 ± 2.3	156.5 ± 1.4	175.2 ± 5.1	55.62 ± 6.51	7.71 ± 1.71	34.75 ± 4.07	4.82 ± 1.07
140430A	1.6	164.4 ± 1.4	171.8 ± 0.4	231.8 ± 2.7	137.25 ± 9.26	21.25 ± 1.70	85.76 ± 5.78	13.30 ± 1.06
140430A	1.6	197.2 ± 1.6	218.5 ± 0.5	365.4 ± 3.5	76.36 ± 2.13	23.75 ± 0.75	47.71 ± 1.33	14.80 ± 0.47
140430A	1.6	17243.3 ± 689.8	18274.6 ± 15.6	20405.3 ± 1299.8	0.20 ± 0.51	2.47 ± 6.91	0.13 ± 0.32	1.55 ± 4.32
140506A	0.889	82.7 ± 0.9	121.9 ± 0.5	226.8 ± 2.3	562.37 ± 13.78	185.84 ± 4.77	113.15 ± 2.77	37.40 ± 0.96
140506A	0.889	198.8 ± 2.9	240.6 ± 1.3	407.1 ± 17.6	68.93 ± 2.27	45.38 ± 2.19	13.87 ± 0.46	9.13 ± 0.44
140506A	0.889	270.4 ± 5.0	345.8 ± 1.1	556.9 ± 5.6	140.59 ± 3.77	103.61 ± 3.12	28.29 ± 0.76	20.80 ± 0.63
140512A	0.725	99.5 ± 1.8	127.9 ± 0.9	176.4 ± 2.3	190.70 ± 9.26	60.24 ± 3.66	25.45 ± 1.24	8.04 ± 0.49
140515A	6.32	1362.1 ± 269.1	2932.4 ± 232.4	15038.4 ± 3379.3	0.21 ± 0.03	9.42 ± 2.39	1.24 ± 0.20	56.30 ± 14.30
140619A	–	100.5 ± 29.4	184.5 ± 13.6	387.9 ± 166.6	77.79 ± 5.32	80.44 ± 11.06	–	–
140619A	–	194.7 ± 6.5	228.6 ± 1.0	949.1 ± 96.5	315.35 ± 41.28	280.84 ± 42.10	–	–
140709A	–	132.9 ± 0.6	139.9 ± 0.3	257.8 ± 6.5	76.12 ± 2.65	19.20 ± 0.84	–	–
140709A	–	142.9 ± 3.2	184.5 ± 0.6	255.8 ± 2.8	101.72 ± 3.78	30.64 ± 1.28	–	–
140709B	–	70.1 ± 6.1	113.0 ± 1.4	392.7 ± 19.8	25.07 ± 0.94	13.59 ± 0.57	–	–
140709B	–	514.4 ± 21.2	545.9 ± 12.4	649.0 ± 50.7	0.63 ± 0.18	0.49 ± 0.26	–	–
140709B	–	834.5 ± 48.1	886.1 ± 33.7	1001.2 ± 84.6	0.32 ± 0.10	0.38 ± 0.31	–	–
140710A	0.558	323.9 ± 13.1	348.7 ± 7.7	792.4 ± 71.6	1.59 ± 0.23	1.95 ± 0.38	0.12 ± 0.02	0.15 ± 0.03
140713A	–	543.1 ± 22.3	667.8 ± 9.6	1392.2 ± 66.8	5.82 ± 0.51	13.04 ± 1.36	–	–
140817A	–	168.5 ± 2.5	207.3 ± 2.4	444.9 ± 44.5	60.56 ± 4.37	49.06 ± 6.82	–	–
140817A	–	245.6 ± 10.8	290.0 ± 2.1	529.3 ± 19.2	24.61 ± 2.85	22.59 ± 3.23	–	–

Table 1—Continued

GRB	z	T_{start} (s)	T_{peak} (s)	T_{end} (s)	F_p (10^{-10}erg cm^{-2} s^{-1})	S_F (10^{-8}erg cm^{-2})	L_p (10^{48}erg s^{-1})	$E_{x,iso}$ (10^{50}erg)
140817A	–	480.6 ± 4.6	509.4 ± 2.1	765.9 ± 18.8	9.81 ± 0.49	10.56 ± 0.83	–	–
140817A	–	722.8 ± 12.7	743.6 ± 6.1	891.7 ± 32.8	4.11 ± 0.77	3.47 ± 1.09	–	–
141005A	–	389.7 ± 3.9E7	396.0 ± 2.5E7	509.6 ± 3E7	0.60 ± 222503.62	0.35 ± 197412.84	–	–
141005A	–	866.7 ± 56.5	1001.8 ± 19.7	1096.9 ± 41.6	1.34 ± 1.00	1.03 ± 0.82	–	–
141020A	–	350.8 ± 0	360.7 ± 0	786.4 ± 99.5	1.30 ± 0	1.69 ± 0.10	–	–
141031A	–	342.5 ± 37.8	454.5 ± 20.6	1447.0 ± 134.7	3.08 ± 0.40	8.87 ± 1.53	–	–
141031A	–	585.8 ± 25.2	796.2 ± 2.8	912.0 ± 3.2	14.81 ± 0.99	13.70 ± 1.03	–	–
141031A	–	762.0 ± 6.5	886.3 ± 1.3	1296.2 ± 15.3	56.92 ± 1.26	52.37 ± 1.22	–	–
141031A	–	977.9 ± 12.5	1098.3 ± 2.4	1606.7 ± 25.9	16.29 ± 0.58	20.23 ± 0.79	–	–
141031A	–	2307.9 ± 3969.5	15369.6 ± 5830.4	293981.7 ± 220593.4	0.02 ± 0.01	18.27 ± 13.47	–	–
141221A	1.452	222.6 ± 34.5	346.8 ± 12.4	536.3 ± 47.5	5.40 ± 0.72	7.39 ± 1.41	2.82 ± 0.38	3.85 ± 0.73
150206A	2.087	1626.1 ± 35.3	2317.5 ± 6.5	3113.3 ± 15.3	58.24 ± 0.92	342.43 ± 8.33	58.86 ± 0.93	346.00 ± 8.42
150222A	–	145.5 ± 4.5	181.4 ± 2.1	233.7 ± 5.5	8.00 ± 0.53	3.31 ± 0.33	–	–
150222A	–	264.4 ± 5.0	284.8 ± 2.1	420.4 ± 11.3	9.46 ± 0.66	4.81 ± 0.45	–	–
150323C	–	64.6 ± 17.0	190.4 ± 1.3	264.3 ± 19.0	29.35 ± 2.15	9.66 ± 0.74	–	–
150323C	–	55.6 ± 10.9	252.1 ± 1.7	676.0 ± 32.5	28.08 ± 0.77	24.69 ± 0.68	–	–
150323C	–	361.4 ± 15.6	401.6 ± 2.8	699.2 ± 54.1	2.18 ± 0.23	1.38 ± 0.16	–	–
150323C	–	580.8 ± 7.6	594.6 ± 0.6	831.5 ± 58.3	0.71 ± 0.16	0.45 ± 0.13	–	–

Table 2. Results of Linear Regression Analysis. The correlations are derived from 200 GRBs with redshifts. R is the Spearman correlation coefficient, P is the chance probability, and δ is the dispersion of correlation.

Correlations	Expressions	R	P	δ
$T_{decay}(T_{rise})$	$\log T_{decay} = (0.77 \pm 0.07) + (0.93 \pm 0.03) \times \log T_{rise}$	0.79	$< 10^{-4}$	0.57
$T_{duration}(T_{peak})$	$\log T_{duration} = (-0.35 \pm 0.11) + (1.12 \pm 0.04) \times \log T_{peak}$	0.78	$< 10^{-4}$	0.55
$L_{\rm p}(T_{\rm peak,z})$	$\log L_{\rm p} = (51.73 \pm 0.17) + (-1.27 \pm 0.08) \times \log T_{\rm peak,z}$	-0.77	$< 10^{-4}$	0.78
$L_{\rm p}(T_{\rm rise,z})$	$\log L_{\rm p} = (50.18 \pm 0.12) + (-0.90 \pm 0.08) \times \log T_{\rm rise,z}$	-0.64	$< 10^{-4}$	0.93
$L_{\rm p}(T_{\rm decay,z})$	$\log L_{\rm p} = (50.47 \pm 0.13) + (-0.77 \pm 0.06) \times \log T_{\rm decay,z}$	-0.67	$< 10^{-4}$	0.91
$L_{\rm p}(T_{\rm duration})$	$\log L_{\rm p} = (50.74 \pm 0.15) + (-0.84 \pm 0.06) \times \log T_{\rm duration}$	-0.68	$< 10^{-4}$	0.89
$L_{\rm p}(E_{\rm x,iso})$	$\log L_{\rm p} = (-4.14 \pm 3.74) + (1.04 \pm 0.07) \times \log E_{\rm x,iso}$	0.71	$< 10^{-4}$	0.86
$L_{\rm p}(L_{\rm x,iso})$	$\log L_{\rm p} = (4.92 \pm 0.82) + (0.90 \pm 0.02) \times \log L_{\rm x,iso}$	0.97	$< 10^{-4}$	0.31
$L_{\rm x,iso}(T_{\rm peak,z})$	$\log L_{\rm x,iso} = (51.96 \pm 0.18) + (-1.38 \pm 0.08) \times \log T_{\rm peak,z}$	-0.77	$< 10^{-4}$	0.84
$L_{\rm x,iso}(T_{\rm rise,z})$	$\log L_{\rm x,iso} = (50.31 \pm 0.13) + (-1.00 \pm 0.08) \times \log T_{\rm rise,z}$	-0.66	$< 10^{-4}$	0.99
$L_{\rm x,iso}(T_{\rm decay,z})$	$\log L_{\rm x,iso} = (50.83 \pm 0.13) + (-0.95 \pm 0.06) \times \log T_{\rm decay,z}$	-0.76	$< 10^{-4}$	0.85
$L_{\rm x,iso}(T_{\rm duration})$	$\log L_{\rm x,iso} = (51.12 \pm 0.14) + (-1.02 \pm 0.06) \times \log T_{\rm duration}$	-0.77	$< 10^{-4}$	0.83
$T_{\rm peak,z}(T_{\rm waiting})$	$\log T_{\rm peak,z} = (0.82 \pm 0.06) + (0.77 \pm 0.03) \times \log T_{\rm waiting}$	0.87	$< 10^{-4}$	0.36
$T_{\rm duration}(T_{\rm waiting})$	$\log T_{\rm duration} = (0.67 \pm 0.12) + (0.81 \pm 0.06) \times \log T_{\rm waiting}$	0.68	$< 10^{-4}$	0.73
$L_{\rm p}(T_{\rm waiting})$	$\log L_{\rm p} = (50.88 \pm 0.14) + (-1.09 \pm 0.07) \times \log T_{\rm waiting}$	-0.74	$< 10^{-4}$	0.82
$L_{\rm x,iso}(T_{\rm waiting})$	$\log L_{\rm x,iso} = (51.02 \pm 0.15) + (-1.17 \pm 0.08) \times \log T_{\rm waiting}$	-0.74	$< 10^{-4}$	0.89